UNIVERSITY OF OKLAHOMA

GRADUATE COLLEGE

AUTOMATED CALIBRATION OF AN ANISOTROPIC MATERIALS

CHARACTERIZATION INSTRUMENT

A THESIS

SUBMITTED TO THE GRADUATE FACULTY

in partial fulfillment of the requirements for the

Degree of

MASTER OF SCIENCE

By

JOEL LOVE
Norman, Oklahoma
2019

AUTOMATED CALIBRATION OF AN ANISOTROPIC MATERIALS
CHARACTERIZATION INSTRUMENT

A THESIS APPROVED FOR THE
SCHOOL OF ELECTRICAL AND COMPUTER ENGINEERING

BY

Dr. Jorge Salazar-Cerreño, Chair

Dr. Binbin Weng

Dr. Caleb Fulton

Acknowledgements

I would like to first thank everyone who helped directly with this thesis. My advisor, Dr. Salazar, took me on as a graduate student even though I work a full-time job and cannot be in the lab as many hours as the other students. I am very grateful for the opportunity to have done this project at all, as many other professors would not have been willing to work around my schedule. Besides providing this opportunity, I am also grateful for his guidance, and feedback throughout the project, and for always being willing to put in a late night to help me figure something out when I needed it. I would like to thank my committee, Dr. Weng and Dr. Fulton, for their time, input, and flexibility as we coordinated the conclusion of this project. I would like to also thank Dr. Qamar for the many hours he spent teaching me about the instrument, running tests with me, and reviewing my thesis, as well as always having some extra food to share when I missed a dinner.

I would like to thank my wife, Brittany, for all of her support and encouragement over these past three years. I certainly could not have made it this far without her. Finally, I would like to thank the rest of the PAARD team, including Dr. Aboserwal, Tom, Kevin, Nim, Rodrigo, Javier, Jose, and Arturo. They have all provided suggestions to me at one time or another, and I enjoyed hearing their weekly updates and seeing their research progress. Watching their projects unfold and seeing their results inspired and motivated me to always push mine further.

Table of Contents

List Of Figures

List Of Tables

Abstract

The increasingly widespread development and use of inhomogeneous composites and artificial dielectrics/diamagnetics has necessitated the development of methods to characterize these materials over a range of frequencies and incidence angles. This paper will present a low-cost ($<$\$10,000) instrument, developed by the Phased Array Antenna Research and Development (PAARD) group at the University of Oklahoma (OU) to perform such material characterization. The proposed RF scanner uses three antennas: one as the transmitter, one as the receiver to measure S_{11}, and one as the receiver to measure S_{21}. The use of two receive antennas allows one to remain stationary opposite the transmit antenna, while the other is free to rotate around the sample at twice the sample's own rotation rate, thereby maintaining a position normal to the surface of the sample. This configuration allows nearly simultaneous measurement of a material's S_{11} and S_{21} at any angle of incidence. High-precision stepper motors, controlled by a Computer Numerical Control (CNC) board as well as rotary tables are used to maintain precise positioning of all three antennas and the rotation of the sample under test. A Graphical User Interface (GUI) has been developed using LabVIEW to automate the calibration and anisotropic material characterization process. The software supports using either Transmission-Reflection-Line (TRL) calibration or Thru calibration to maintain the system's accuracy. The Smith algorithm is then used to calculate the material's permeability and permittivity at all incidence angles from the measured S-parameters, producing plots of the real and imaginary parts of the permeability and permittivity versus angle of incidence. The system has been

confirmed to accurately measure the permittivity and permeability of FR4, Rogers 4350B, Rogers 5880, and Rohacell at broadside, as well as the permeability and permittivity for FR4 and an anisotropic engineered material (frequency selective surface) at multiple angles of incidence.

Chapter 1

Introduction

1.1 Motivation

Radio frequency (RF) technology has improved significantly in the past decades since the first radio was fabricated, increasing in capability and shrinking in size, but also increasing significantly in complexity. Modern RF devices have pushed conventional design methodologies to their limits, and as the requirements for these devices grow ever more strict, new and better approaches must be explored. One aspect of RF design currently under study is the customization of the dielectric materials used in RF circuits. Introducing anisotropic properties into the dielectric materials allows additional freedom in RF circuit design, and will allow even stricter requirements to be met. However, while the processes to design and fabricate these engineered dielectrics are developed, a convenient, high-performance tool will be needed to measure the properties of these materials with respect to frequency and angle-of-incidence. A previous design, conducted by Alex Stringer at the Advanced Radar Research Center, produced a proof-of-concept for such a tool that covers a frequency band of 2-10 GHz [2]. This thesis documents upgrades made to this machine to improve its accuracy, repeat-ability, and convenience, through robust calibration, hardware improvements,

and automated software. When finished, it should be ready for use as an everyday materials-characterization machine in a rapid-prototyping lab setting.

1.2   Literature Review

Since the free-space materials characterization instrument was already designed and fabricated, this thesis is primarily concerned with the modifications to perform absolute calibration, and post-processing to obtain accurate measurements of electrical material properties (relative permittivity, relative permeability, and loss tangent). Calibration methods considered include Transmission-Reflection (TR) and Transmission-Reflection-Line (TRL), which are the most commonly used calibration methods in similar free-space materials characterization instruments [4]. TR calibration is described in [5] and [4], and TRL is described in [6]. The system's vector network analyzer (VNA) is used to save the calibration parameters and calculate the calibration coefficients. Calibration of VNAs is described in [7], [8], [9], [10], and [11]. While calibrating the VNA is critical in improving the accuracy of our results, there can still be significant error in data, stemming from a variety of sources, as described in [4]. One significant source of error are multipath signals reaching the receive antenna. These signals can be filtered out using a properly configured time-gate, set on the VNA, as described in [12] and [4]. However, the time-domain resolution, and therefore the effectiveness of the time-gate, depends on the bandwidth of the frequency sweep: the greater the frequency sweep, the better the time-gate, as described in [4].

Once the most accurate data possible is collected, permeability and permittivity can be calculated using any of a selection of different extraction algorithms. Extraction algorithms fall into two main categories: direct algorithms, which calculate permeability and permittivity directly from the data, and iterative algorithms, which must calculate permeability and permittivity numerically, often using some form of numerical root-finding technique. The more common extraction algorithms used are described in [11], [4], and [13]. Direct algorithms used in this project include the Nicolson-Ross-Weir (NRW) method, described in [14], and [15] and the Smith algorithm, described in [16]. These algorithms are simpler to implement in Matlab than an interative algorithm since they do not require the use of numerical techniques to ensure they converge, but they do have some other disadvantages, namely they produce multiple possible solutions. The correct solution can be chosen if an approximate value for it is known *a priori*; otherwise more complicated approaches can be used, such as the Kramers-Kronig integral, described in [17], [18], [19], [20], [21], and [22], or phase unwrapping, described in [23] and [24]. However, the main disadvantage encountered in this project is the inability to calculate only permittivity from measured S21 using the direct algorithms. The measured S11 data often contains more error than the measured S21 values, and the permeability is often known to be 1, so if possible, calculating permittivity only from S21 would improve the accuracy of the results. Iterative algorithms, on the other hand, can calculate permittivity only using S21 data. They also do not produce multiple solutions, so there is no ambiguity as to the correct solution. Their downsides include increased complexity, making them more difficult to implement, and they may not converge to any solution depending on

the algorithm's starting guess and the specific numerical convergence technique used. Iterative extraction algorithms are described in [25], [26], [27], [28], and [29].

1.3   Problem Statement

The main goal is to improve the accuracy of the system's calibration, and to allow convenient 2-D measurement of anisotropic materials. The previous system design proved the concept of an anisotropic materials characterization instrument by taking several samples manually at a few angles of incidence, but the upgraded system will need to perform much finer angular sweeps, at a higher degree of accuracy. Since calibration will need to be performed at each angular position tested, the calibration process, antenna switching process and the angular sweep itself, will need to be fully automated. This will require significant system modification, but will increase its accuracy and ease of use as a laboratory instrument.

1.4   Organization of the Thesis

This thesis is organized as follows. It begins in Chapter 2 with a review of the existing anisotropic materials characterization instrument, designed and fabricated prior to the start of this project by Alex Stringer and the Phased Array Antenna Research and Development group (PAARD). The general electromagnetic and materials characterization theory, as well as the calibration techniques employed, are also reviewed. Chapter 3 covers the hardware modifications and upgrades performed to the system to allow full automation of the system, and improve its accuracy. Chapter 4 covers

each of the electrical subsystems to be controlled, how each can be controlled by the central computer, and the details of the LabVIEW code for how the program actually performs the desired control. Chapter 4 also presents the results obtained from the instrument's characterization of several known samples, in both the broadside configuration (normal incidence) and with a 60 degree angular sweep (oblique incidence). Finally, chapter 5 presents suggestions for improving the design to further reduce error, as well as the final project conclusions.

Chapter 2

Review of Previous Work

2.1 Introduction

Since this thesis builds heavily upon work previously done, Chapter 2 will focus entirely on reviewing the theory behind the original machine design and the design details of the machine as previously manufactured. Additionally, the free-space calibration techniques used to calibrate this system are covered, and their individual benefits and drawbacks are discussed. With this background information established, understanding the modifications performed to the system to facilitate its automation will be much simpler in Chapters 3 and 4.

2.2 Free-Space Method for Materials Characterization

The free space method uses antennas connected to a vector network analyzer to measure the S-parameters of a slab of material, as shown in Figure 2.1. These S-parameters can then be used to calculate the material's constitutive parameters. This technique was chosen because of its flexibility to easily support mechanical changes in sample orientation, since the sample is separated from the transmit and receive antennas by open space. This method has also been the subject of significant study, and as such, it is well understood what is required to obtain accurate results. The

main assumption made when extracting the constitutive parameters using the free-space method is that the measured S-parameters are only the result of the excitation waves reflecting off of, or transmitting through the material under test as plane waves. Anything that degrades this assumption introduces unwanted errors into the result. A thorough discussion of potential error sources unique to the free-space method and measures taken to mitigate them follows.
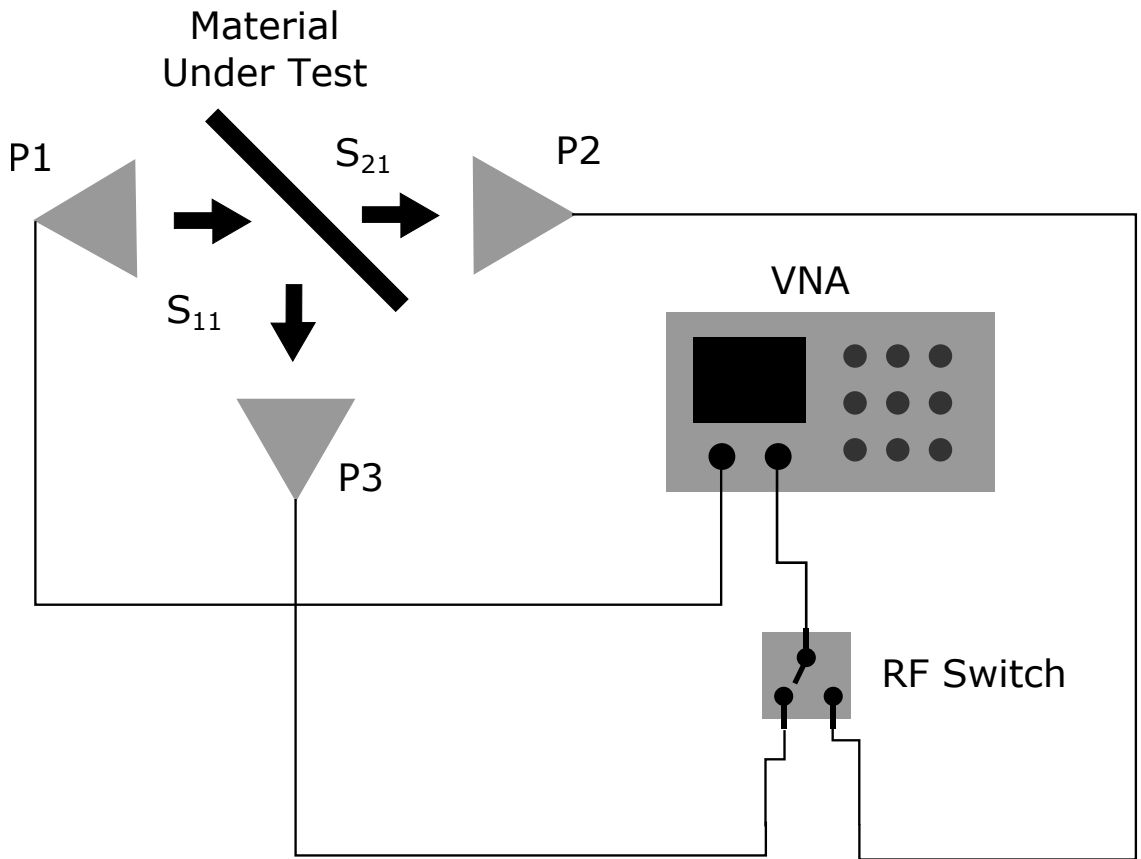
Figure 2.1: Free space characterization - oblique incidence.

First, in order to maintain our assumption that the excitation signal only interacts with the material under test, great care must be taken that the entire antenna beam area strikes the sample. Should some portion of the beam pass over the edge of the sample and travel directly to the receive antenna, the sample's transmittance

will be overestimated, while its reflectance will be underestimated. Additionally, even if the beam is too close to the sample edge, reflections can occur off of the edge at unpredictable angles, potentially reflecting back into the transmit antenna and introducing error into the measured reflectance, or being absorbed by the surroundings, causing the material's loss to be overestimated. For this reason, the sample's width and height should be at least 1.5 times the antenna beam's width and height at the distance the measurement will be performed [4]. Since an antenna's area of illumination increases with distance, and the required sample size is desired to be minimized in order to reduce cost, highly directive antennas with very narrow beam-widths are most suitable for this application.

However, because the free-space approach also assumes that only plane waves strike the sample, the antenna must be far enough away from the sample that it is in its far-field region. If it is not, phase errors will be introduced, reducing the accuracy of the measured constitutive parameters [4]. This requirement is at odds with the desire to minimize the required sample size by positioning the sample as close to the antenna as possible. Some antenna designs can reach far-field behavior in relatively small distances, but typically dielectric lenses are used to focus the antenna beams into a Gaussian beam. The Gaussian beam's width will taper versus distance to a minimum at the focal point, after which it will begin increasing. At this focal point, the beam will have a constant phase front. So as long as the sample is placed at the beam's focal point, the sample size can be maintained at a minimum while the constant phase front assumption is maintained.

All these error sources were considered during the previous system design, discussed later in this chapter, and were further mitigated through hardware modifications, as discussed in Chapter 3.

2.3   Free-Space Calibration Techniques

Besides controlling these external error sources, the free-space materials characterization instrument must be properly calibrated in order to eliminate the effects of the cables routing the vector network analyzer (VNA) signals to the antennas, the antennas themselves, and any additional hardware implemented between the VNA's ports and free space. There are several different VNA calibration techniques, but the two used in this system: Thru-Reflect-Line (TRL), and Thru, are discussed below.

2.3.1   TRL Calibration

TRL calibration builds a pair of error boxes as a model to describe everything connected to the VNA ports. The method then measures the S-parameters of these error box models using calibration standards which are assumed to be perfect. TRL calibration is normally performed on a VNA with all cables and other hardware that will be used during the measurement, connected. The calibration itself is performed in three separate stages. First, for the thru measurement, the two ports of the VNA are connected directly together and the the results are sampled at the VNA's ports, as shown in Figure 2.2.
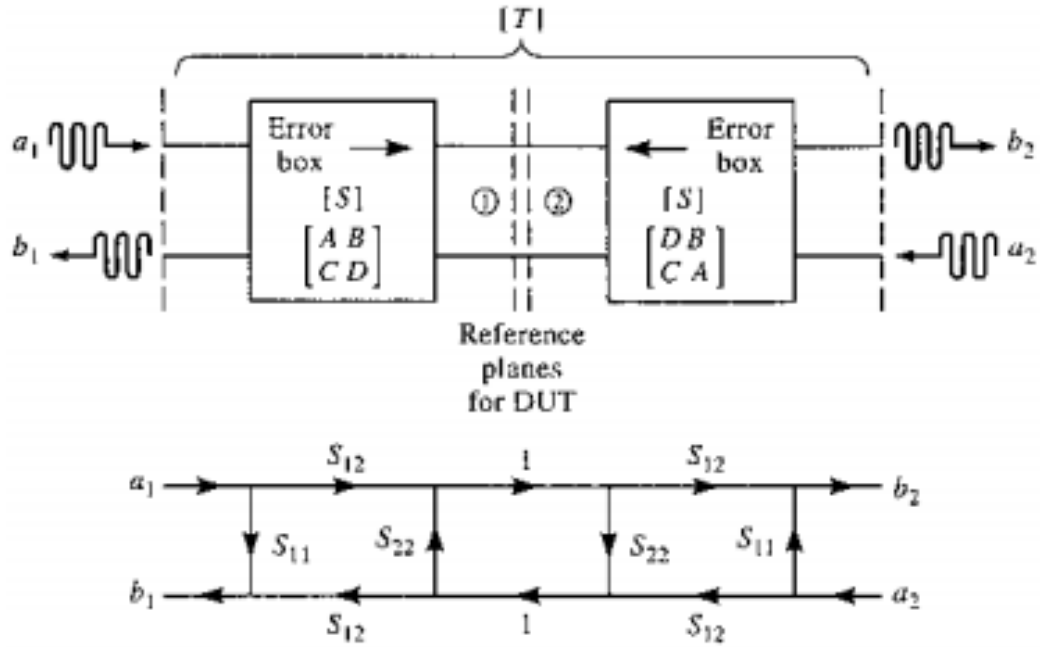
Figure 2.2: TRL Calibration - Thru [1]

T_{11}, T_{12}, T_{21} and T_{22} results obtained from this measurement can be equated to the S-parameters of the error boxes using the following formulas. For symmetric and reciprocal systems, of which the free space materials characterization instrument is one, $T_{11} = T_{22}$, and $T_{21} = T_{12}$ [1].

$$T_{11} = S_{11} + \frac{S_{22}S_{12}^2}{1 - S_{22}^2}we \qquad (2.1)$$

$$T_{12} = \frac{S_{12}^2}{1 - S_{22}^2} \qquad (2.2)$$

In a free-space system, since antennas are used rather than coaxial cable ports, the thru calibration can be performed by properly connecting all system hardware, positioning the antennas at the desired positions for sample measurement (such that the antennas have a direct path to each other), and taking the calibration. Care

should be taken to ensure the antennas are as mechanically aligned with each other as possible, as any misalignment between the antennas degrades the assumption that a perfect thru is used. Additionally, the antennas should be kept at identical distances from the sample holder, as any difference in the distances to the sample holder degrades the assumption that the system is symmetric.

The next step in a TRL calibration is the reflect stage. For this stage, a perfect reflect standard is placed between the ports of the VNA, as shown in Figure 2.3.
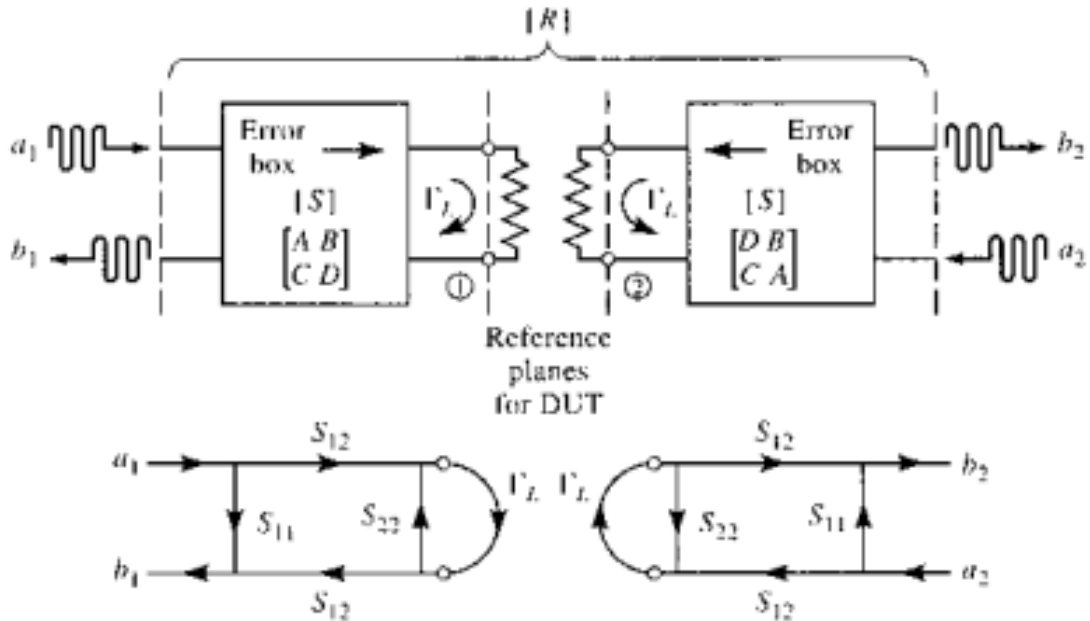
Figure 2.3: TRL Calibration - Reflect [1]

In this stage, only R_{11} and R_{22} need to be measured, since R_{12} and R_{21} are assumed to be zero. Once again, $R_{11} = R_{22}$ by symmetry. This yields the following relationship in terms of the error box S-parameters [1].

$$R_{11} = S_{11} + \frac{S_{12}^2 \Gamma_L}{1 - S_{22}\Gamma_L} \tag{2.3}$$

In the special case of a free-space system, after performing the thru calibration and keeping the antennas in the same position, the reflect standard can be inserted into the sample holder and the reflect calibration taken. A reflective sheet of copper, or a double-sided copper clad board of identical thickness to the sample can be used as the reflect standard. It's width and height, like the sample, should be at least 1.5 times the antenna's beam-width at the measurement position to ensure that all radiant energy is reflected. Should an undersized reflect standard be used, some radio frequency (RF) energy could travel directly between the VNA ports, thus degrading the assumption of complete isolation between the ports.

The final stage of TRL calibration is the line standard. This standard inserts a 90 degree (quarter wavelength) section of transmission line between the VNA ports as previously calibrated, as shown in Figure 2.4.
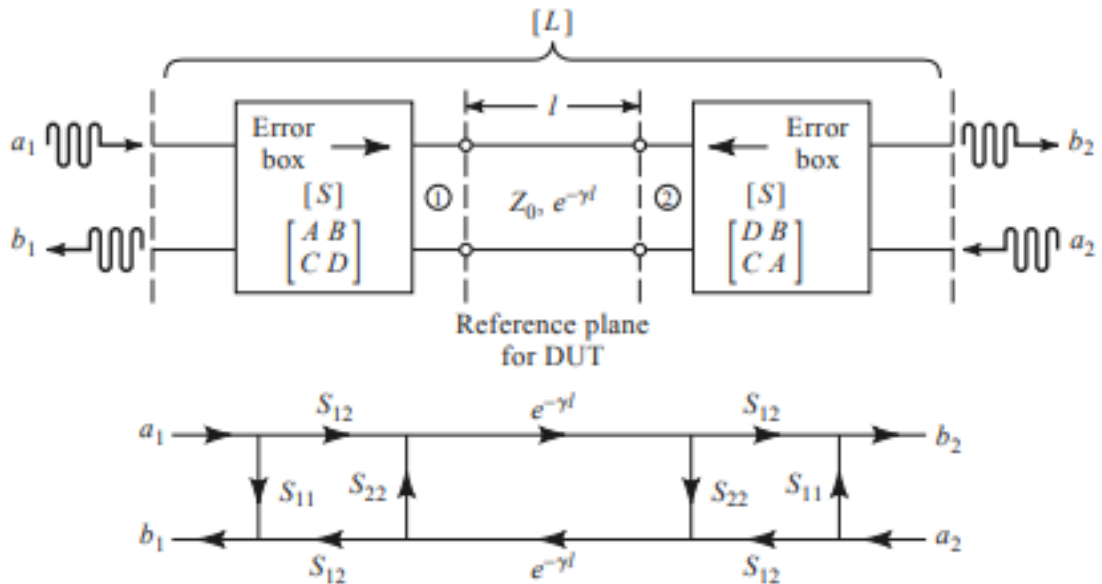
Figure 2.4: TRL Calibration - Line [1]

In this stage, L_{11} and L_{12} are measured, and again by symmetry and reciprocity it is assumed that $L_{11} = L_{22}$ and $L_{12} = L_{21}$. This yields the following relationship [1].

$$L_{11} = S_{11} + \frac{S_{22}S_{12}^2 e^{-2\gamma l}}{1 - S_{22}^2 e^{-2\gamma l}} \tag{2.4}$$

$$L_{12} = \frac{S_{12}^2 e^{-\gamma l}}{1 - S_{22}^2 e^{-2\gamma l}} \tag{2.5}$$

In the case of free-space calibration, we can now remove the reflect standard from the sample holder, and we must increase the distance between the two antennas by 90 degrees. Depending on the frequency we are testing the sample at, this distance will change. If the testing is to be performed over a wide frequency range, multiple line samples should be taken to prevent a 180 degree phase shift in the measurement band [4]. Once the antennas have been separated by an additional 90 degrees and the line standard taken, they should be returned to their original positions as accurately as possible, as any deviation in the antenna position from where the thru and reflect standards were taken will add error into the final results.

For calibration purposes, the TRL line standard should apply a perfect 90 degree phase rotation without affecting magnitude at all, relative to the thru standard. However, increasing the distance between the two antennas in a free-space approach does affect the magnitude relative to the thru standard because of path loss. Path loss describes the attenuation to a signal when propagating through free space, and is given in the below formula. How much the magnitude is affected depends primarily

13

on the distance from the sample at which the thru standard is taken. If this distance is significant relative to a quarter wavelength (which it must be for the antenna to be in the far-field), then the difference in path loss will be minimal. This affect is assumed to be negligible for the remainder of this thesis [1].

$$L_0(\text{dB}) = 20 \log_{10}\left(\frac{4\pi R}{\lambda}\right) \tag{2.6}$$

With all three steps completed, there is now enough information to solve for all the S-parameters of the error boxes. Since the error boxes are a model for the VNA cables, the antennas, and any other hardware between the VNA ports and the sample, we can now remove their effects from the sample data. But it is important to remember that if the system changes in any way after the calibration is performed, it will not be captured in the error box model without re-calibrating the system, and thus contribute directly to errors in the calculated material constitutive parameters.

With three separate stages, the insertion and removal of calibration standards, and, for free space, the precise positioning of the antennas at multiple positions, makes TRL calibration fairly complicated and time consuming. It is, however, a very accurate way to calibrate a system, and calibrates for all parameters on a two-port VNA. For these reasons, if TRL calibration is to be used, extra care must be taken during the system design to ensure it can be conveniently performed.

2.3.2   Thru Calibration

Thru calibration is performed identically to the thru stage of TRL calibration with no additional steps taken. On its own, thru calibration does not provide enough information to calibrate the VNA in both S_{11} and S_{21}, or, of course, enough information to fully characterize a full error box model of the system. Instead, it simply zeros the S_{12} and S_{21} readings. This method will not be as accurate as a full TRL calibration, but can also be performed much more quickly, requiring only one step and no insertion of any standards or in the case of free-space calibration, any change in antenna positions. For these reasons, it only makes sense to use thru calibration if time or system complexity prevent the use of a more robust calibration, like TRL [1].

2.4   Legacy System Design

The legacy system utilized a Computer-Numerical-Control (CNC) frame from Open-Builds, as shown in Figure 2.5. This frame consisted of six separate aluminum rails, each with a lead screw along its length, fixed to a mount at either end. The lead screw is threaded through a trolley with four wheels that slot into the side of the aluminum frame, such that rotating the lead screw moves the trolley along the length of the frame. National Electrical Manufacturers Association (NEMA) 23 stepper motors are then mechanically coupled to the lead screws, allowing electronic control over the screws' rotation. Two of the rails are mounted to a single rod in the center of the machine and fixed to the table opposite one another, while the third arm is pinned to the same central rod, but not fixed at a second point, thereby allowing it to rotate

about the central rod. The three remaining rails are then mounted to each of the three trolleys, forming three axes perpendicular to the original three, which the system's probes mounted to their respective trolleys. In this way, all three antennas can be moved in or out with respect to the center of the machine, and up and down with respect to the table, with the third arm also being free to rotate about the machine's center point, but remaining in the plane of the table. The in-and-out and up-and-down movement of the antennas is controlled precisely by the TinyG CNC controller, and can be easily automated with software by sending commands over the TinyG's Universal Serial Bus (USB) port. However, in this original design, the P3 (Figure 2.1) receive antenna must be manually moved for each angular data point desired. Several angular points were measured and guides marked on the table as an assist in aligning the antenna at these angles, but there can still be significant human error in performing this alignment. Automating the movement of this arm with stepper motors would improve the accuracy of the antenna placement, greatly increase the number of discrete angles that can be measured, and reduce the time required for this action to be performed.

The TinyG CNC control board was selected to control all of the NEMA 23 stepper motors. This is a low-cost control board that provides up to four separate channels to control up to four different axes. Since there are six separate motors to drive, all motors cannot be driven individually with a single board, so the three in-and-out axes were wired together as a single axis, and the three up-and-down axes were wired together as a second axis. Additionally, the control board is incapable of driving the motors directly, so six DQ542MA stepper motor drivers were purchased to form a

layer between the control board and the motors. The wiring of this system is shown

in Figure 2.6.
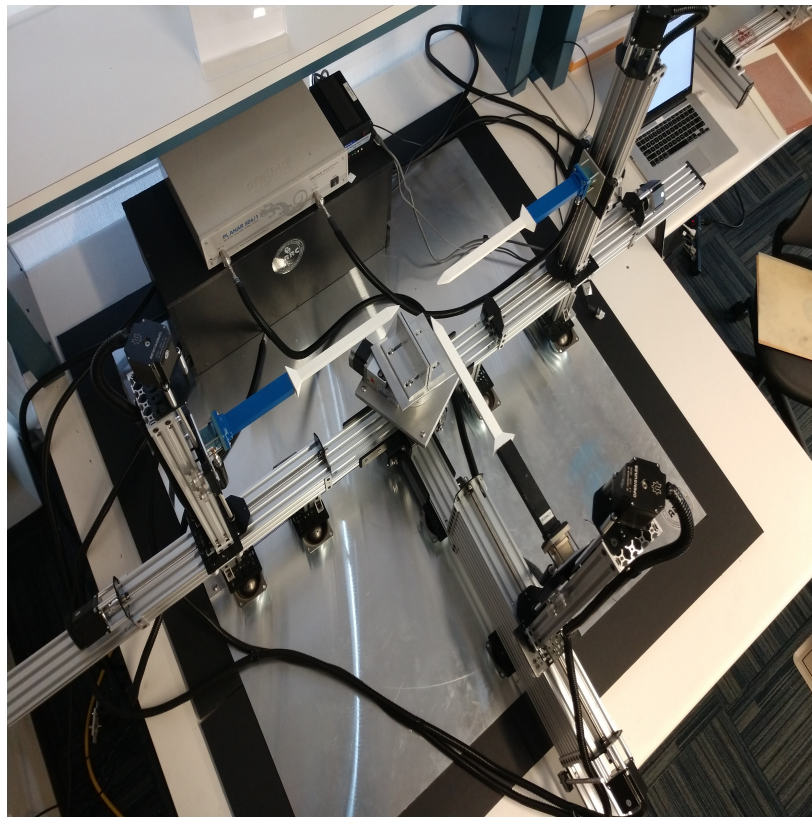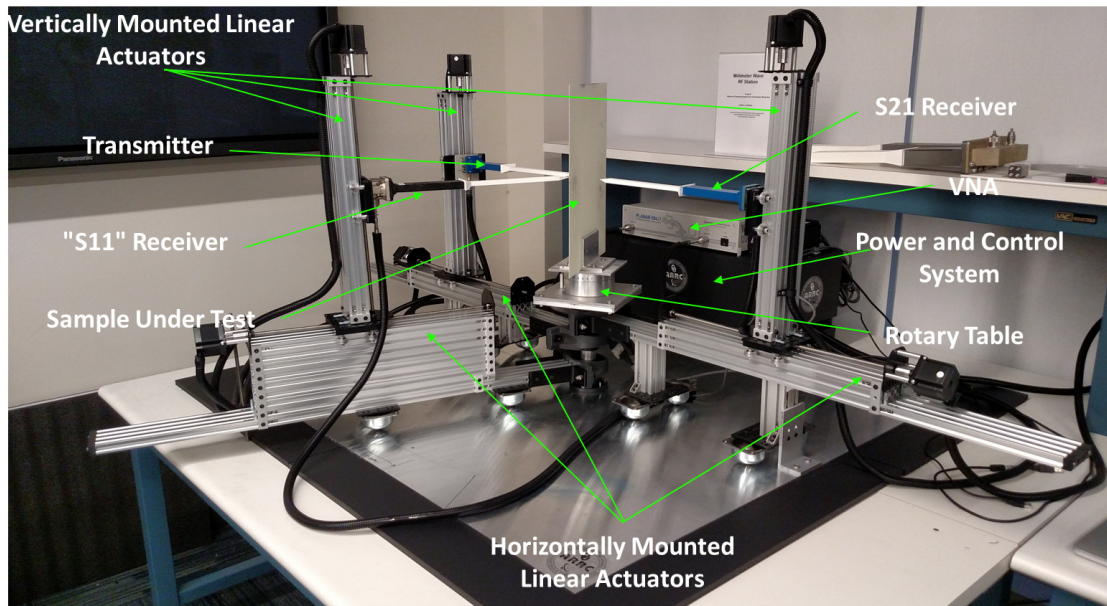
Figure 2.5: Legacy system. [2]
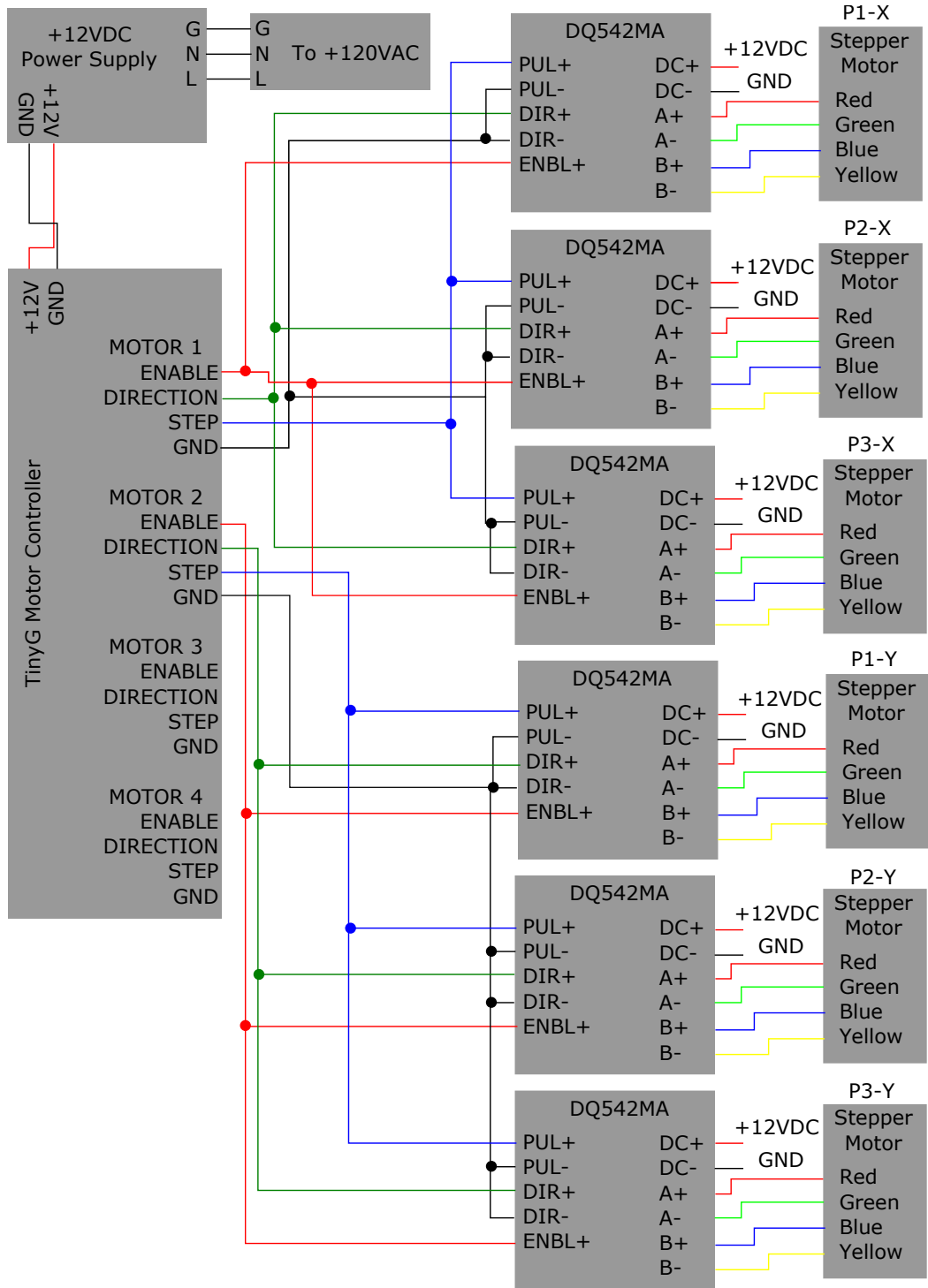
Figure 2.6: Schematic of legacy system wiring.

A two-port Copper Mountain Planar 804/1 VNA was used for calibration and data collection. Because this VNA only has two ports, but three probes are used, the

probes must be manually connected to and disconnected from the VNA to measure a sample's transmitted and reflected signals at oblique angles of incidence. This can be quite time consuming should measurements at a large number of discrete angular points be desired. For this reason, an automated way of switching between the two receive antennas will be a necessary upgrade.

The probes used were custom polyrod antennas, which were characterized in an anechoic chamber. These antennas do not have as constant a wave-front as that produced by dielectric lenses, but it is still quasi-constant over the sample region when positioned at an appropriate distance from the sample, as discussed in Chapter 4 and shown in Figure 4.24 [2], [30], [31], [32].

2.5 Summary

This chapter reviewed the work done previously on the development of the anisotropic materials characterization instrument. To begin, the free-space materials characterization process was described from a theoretical standpoint, including its advantages, disadvantages, and why it was ultimately selected for this instrument. Next, several techniques for accurately calibrating a free-space materials characterization instrument, which were determined to be the most appropriate for this system, were described. The details of how they are implemented into the modified system will be covered in Chapter 4. Finally, the details of the legacy system were provided, including the mechanical design, electrical design, and system schematics. Several characteristics of the system that would require modification in order to automate

the process were also pointed out. This provides a solid base from which to begin modification and improvement of the system.

Chapter 3

System Hardware Modifications and Upgrades

3.1 Introduction

As stated in the previous chapter, the previous design successfully proved the concept of a free-space anisotropic materials characterization instrument, but would need several hardware modifications to allow fully automated testing. This chapter documents all hardware changes made to the system, and how they will facilitate its automation with appropriate software.

3.2 Electrical Modifications

All modifications performed to the system can be broken into two categories - electrical modifications, including new circuitry added and rewiring performed, and mechanical modifications, including new bracket design and mounting. Each is discussed individually below.

3.2.1 Integration of Second Control Board

The original instrument design utilized a single TinyG v8 Computer Numerical Control (CNC) board to control the six DQ542MA stepper motor drivers, which in turn drove six stepper motors - one for the in-and-out axis of each of the three arms, and

one for the up-and-down axis of the arms. The TinyG v8 board allows control of up to four axes, mapped to X, Y, Z, and A. The original configuration wired the TinyG's X-axis output to three DQ542MA stepper motor drivers which in turn were wired to the three in-and-out motors, and its Y-axis output to the three remaining DQ542MA stepper motor drivers connected to the three up-and-down motors. This configuration allowed control of all six motors while only using two of the TinyG's control channels, which would simplify the control software, and theoretically should keep all antenna arm positions at the same position relative to each other. However, over time, should any slop in the system cause one arm to become offset from the others, someone would need to manually correct the motor's position, which would be a difficult and time-consuming process. In order to remove this possibility and provide the user greater control over the system, a second TinyG control board was purchased and the system was rewired to allow individual control over each of the system's six axes. The mapping of each of the axes to the board channel controlling them is shown in Table 3.1, the TinyG v8 pinout is given in Figure 3.1, and the complete schematic is given in Figure 3.2.

Antenna	Board Number	Axis
P1X	Board 1	X
P1Y	Board 1	Y
P2X	Board 1	Z
P2Y	Board 2	X
P3X	Board 2	Y
P3Y	Board 2	Z

Table 3.1: Antenna to TinyG axis mapping.
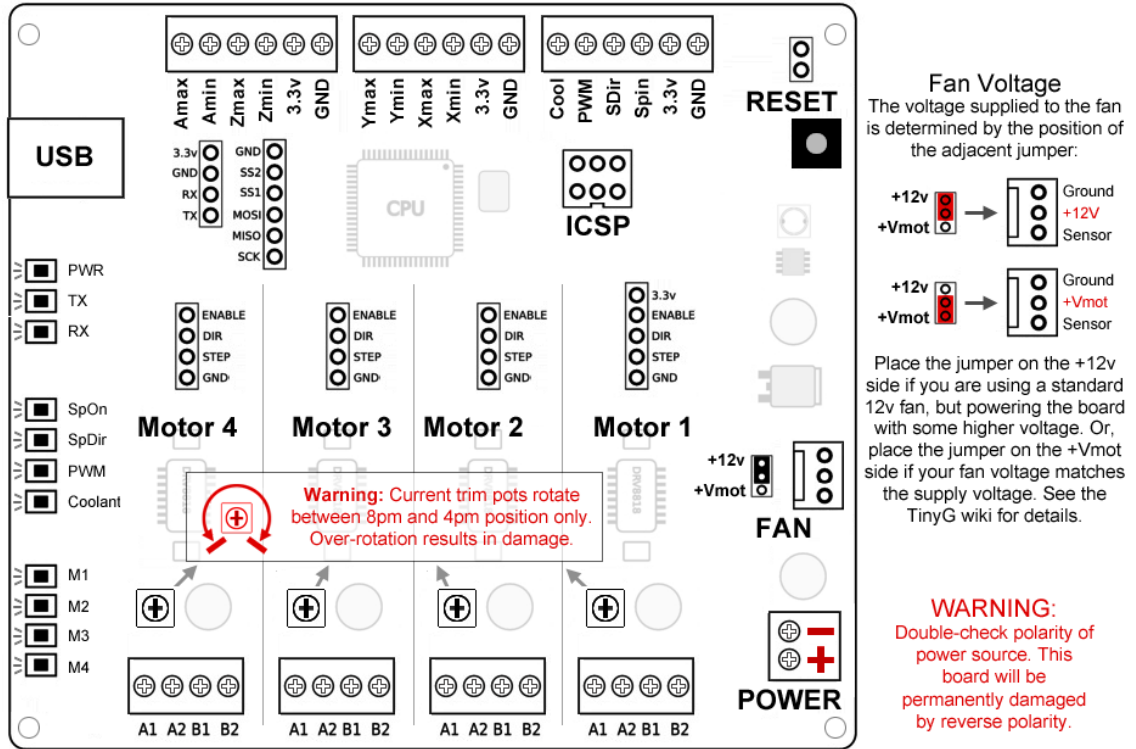
Figure 3.1: TinyG v8 Pinout. Copyright Synthetos.com
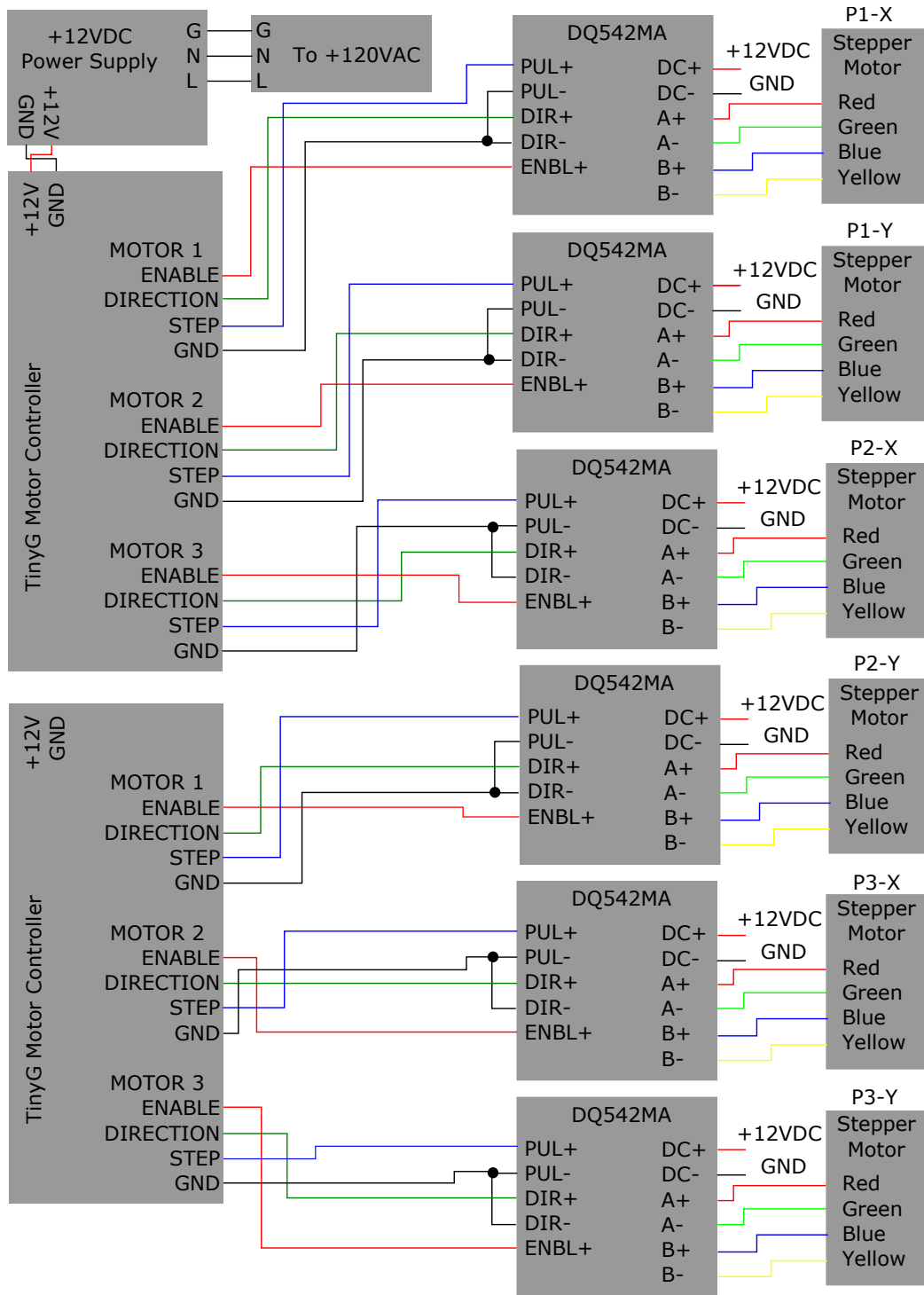
Figure 3.2: Schematic of new system wiring.

3.2.2   Integration of Limit Switches

The addition of the second TinyG control board and rewiring the system allowed individual control of each of the arms, but a controlled procedure was still needed to move the arms to a known starting position. Without such a procedure, the system would have to assume the arms were at the zero position whenever the software is run, which could cause the system to run the arms into a stop if they were not in the assumed starting position. OpenBuilds limit switches (Figure 3.3) were selected to provide the feedback necessary for a homing system. One switch was installed at the lowermost position of each of the up-and-down axes, and the outermost position of each of the in-and-out axes. Each switch was then wired to either the Xmax or Xmin screw terminal (where X represents either the X-, Y-, or Z-axis) of the apporpriate TinyG board in the following pattern. Each of the two Z-axis switches were wired to the Zmax position, while the X- and Y-axis switches were wired to either the Xmin or Ymin positions, corresponding to the axis of control, as summarized in Table 3.2. This somewhat unusual axis definition was chosen to accommodate the TinyG's firmware. The TinyG control board is primarily used in 3-D printer or milling machine configurations where the Z-axis corresponds to a tool's vertical position, and the X- and Y-axes lie in the plane of the table. Typically in an application like this, it is desirable for the tool to lift to its maximum height off the table before moving to its home corner, so that it does not collide with any parts that might be on the table. Originally, it seemed preferable to configure the switches so that all axes were defined with the limit switches at the minimum position, but due to a bug in the TinyG's

firmware, this configuration causes the homing operation to consistently fail. This bug was reported to the TinyG support staff, but since the software is maintained by the community, it could be some time before a fix is implemented. However, by defining the axes so that their directions correspond to the traditional milling machine configuration shown in FIGURE X, we can "trick" the TinyG into performing the desired homing operation, we will just need to remember this axis orientation when controlling the arms later. The complete schematic of the TinyG limit switch wiring is shown in Figure 3.4.

Figure 3.3: Limit Switch. Copyright © 2019 OpenBuilds Part Store

Antenna Limit Switch	Board Number	TinyG Pin
P1X	Board 1	Xmin
P1Y	Board 1	Ymin
P2X	Board 1	Zmax
P2Y	Board 2	Xmin
P3X	Board 2	Ymin
P3Y	Board 2	Zmax

Table 3.2: Limit switch to TinyG axis mapping.
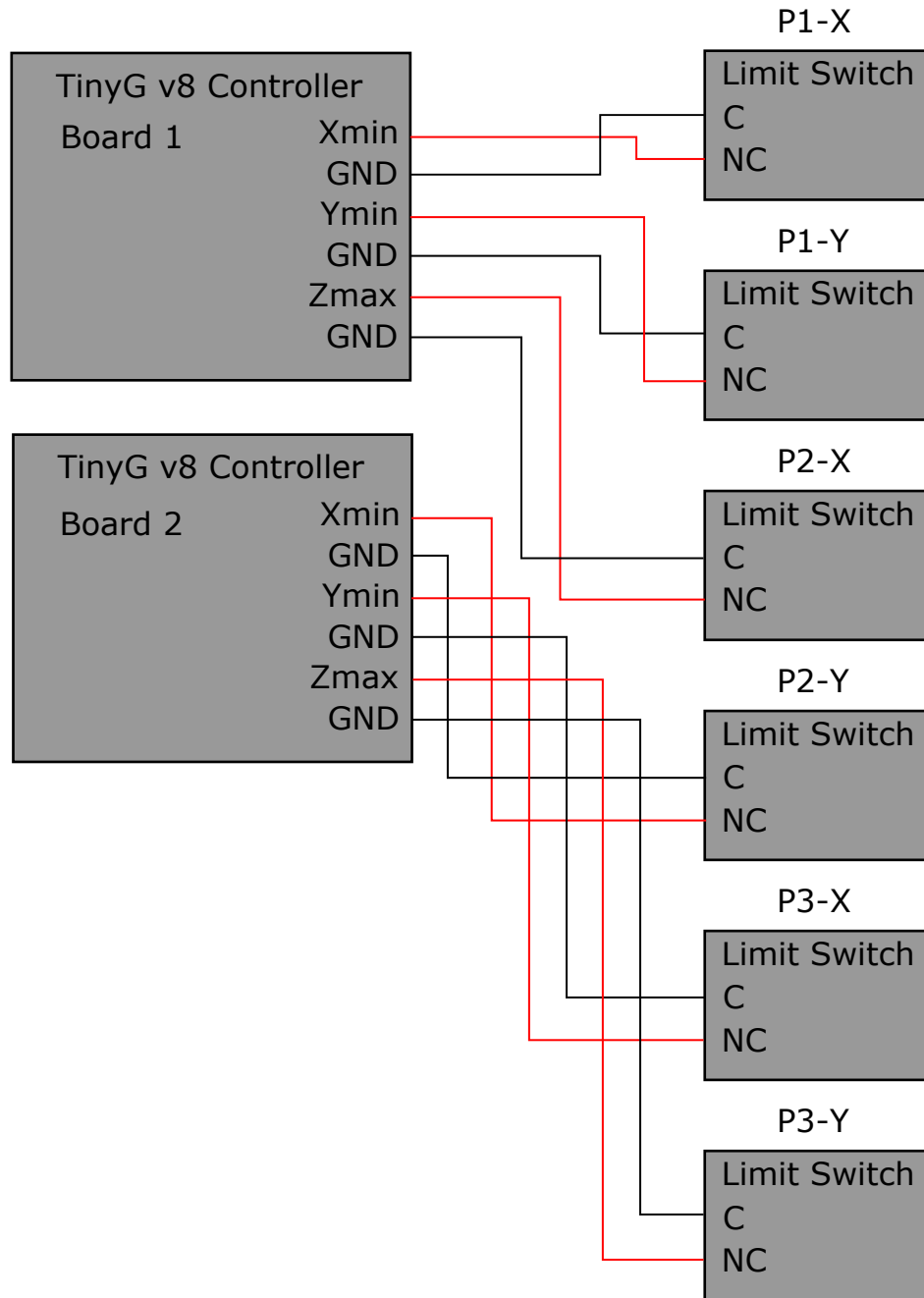
Figure 3.4: Wiring of the TinyG v8 and limit switches.

Once the limit switches were installed, a laser-level and tape measure were used to ensure that all limit switches were positioned at the same height, and at the same distance from the center of the sample holder. Over the course of the system's life, if

the limit switches are bumped or otherwise moved, their positions will need to be re-calibrated, as they directly impact the accuracy with which the antenna positions can be set. But as long as the switches remain in their calibrated location, the antenna positions will be accurately and easily re-calibrated every time the system is run.

With the limit switches properly installed, the TinyG could then be configured to perform the desired homing operation. The available properties and the values they are set to are summarized in Table 3.3. Once the TinyG control boards were configured, the homing operation was tested and verified to be working properly.

3.2.3 Radio Frequency (RF) Switch Control

A Mini-Circuits MTS-18XL-B RF switch had been previously selected to allow au-tomatic switching between the P2 and P3 antennas. This switch provides 85 dB isolation between the disconnected terminals, 0.2 dB insertion loss, and can handle up to 10 W of power. It is shown in Figure 3.5. When properly connected to the an-tennas and vector network analyzer (VNA), the switch can be used to select between the two antennas by applying 24 VDC or ground to its control terminals. 24 VDC is readily available from a DC power supply in the controls cabinet since it is used for the TinyG v8 and the stepper motors, but a convenient way to switch this voltage on and off to the RF switch was still needed.

Command	Description	Value
$ST	Switch Type: 0 for normally open, 1 for normally closed	1
$XSN	X Minimum Switch Mode: 0 for disabled, 1 for homing, 2 for limit, 3 for limit and homing	3
$XSX	X Maximum Switch Mode: 0 for disabled, 1 for homing, 2 for limit, 3 for limit and homing	0
$YSN	Y Minimum Switch Mode: 0 for disabled, 1 for homing, 2 for limit, 3 for limit and homing	3
$YSX	Y Maximum Switch Mode: 0 for disabled, 1 for homing, 2 for limit, 3 for limit and homing	0
$ZSN	Z Minimum Switch Mode: 0 for disabled, 1 for homing, 2 for limit, 3 for limit and homing	0
$ZSX	Z Maximum Switch Mode: 0 for disabled, 1 for homing, 2 for limit, 3 for limit and homing	3
$xSV	Search Velocity: Sets the velocity when searching for the limit switch, where x can be either X, Y, or Z.	30
$1po	Polarity: Sets the polarity for motor 1, 0 for clockwise rotation, 1 for counter-clockwise rotation	0
$2po	Polarity: Sets the polarity for motor 2, 0 for clockwise rotation, 1 for counter-clockwise rotation	0
$3po	Polarity: Sets the polarity for motor 3, 0 for clockwise rotation, 1 for counter-clockwise rotation	0

Table 3.3: TinyG v8 limit switch configuration settings. Copyright Synthetos.com

Figure 3.5: RF Switch. Copyright © 2017 Mini-Circuits

Some kind of microcontroller would be needed for the computer to communicate with directly, but 24 VDC is a relatively high voltage for a microcontroller to switch natively, so a relay would be needed that could accept a 0-5 VDC control signal from the microcontroller, and switch 24 VDC to the relay. The Crydom DC60S3 solid-state relay was selected to perform this function. It is shown in Figure 3.6 and its specifications are summarized in Table 3.4.

Figure 3.6: Solid-state Relay. Copyright © 1996-2019 Crydom, Inc.

Property	Value
Control Voltage	3.5-32 VDC
Control Current	2.2-25 mA
Load Voltage	3-48 VDC
Load Current	3 A

Table 3.4: Crydom DC60S3 Solid-state Relay Specifications.

The microcontroller, then, did not have any special requirements, it only needed to be able to provide a 3.5-32 VDC signal to turn the solid-state relay on or off, and have a Universal Serial Bus (USB) or Universal Asynchronous Receiver-Transmitter (UART) interface to accept commands from the computer. Nearly any microcontroller available would satisfy these requirements, so the Arduino Uno Wifi Rev 2 using the Atmel ATMEGA4809 microprocessor was selected as a simple off-the-shelf

option. The Arduino Integrated Development Environment (IDE) is easy to use and has lots of community support, which would allow more rapid development of its firmware. The board is shown in Figure 3.7. The final wiring of the RF switch, solid-state relay, and Arduino Uno is shown in Figure 3.8.

Figure 3.7: Arduino Uno Wifi Rev2. Copyright © 2019 Arduino
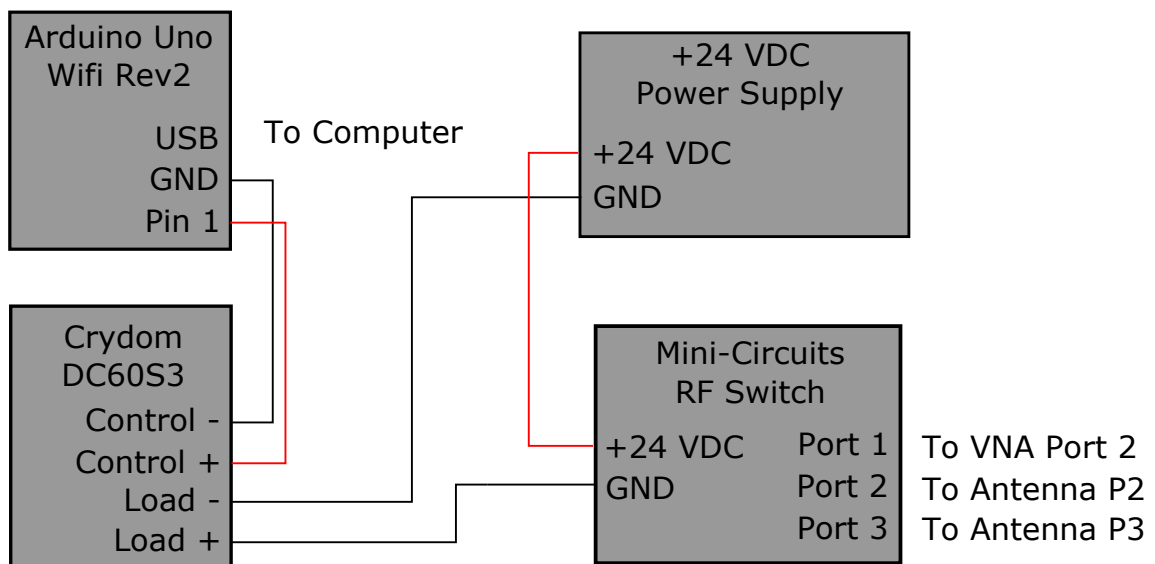
Figure 3.8: Rf Switch Controller Schematic

3.3 Mechanical Control of Third Arm

The original system design allowed the third arm to be rotated around the sample on its ball-transfer supports. This method required manually loosing the arm's stop, positioning the arm for a given angular sample, and tightening the stop to hold it in place. Manually moving the arm for every sample is both time consuming and inaccurate, so a hardware upgrade was needed to allow automation of this process. Several options were proposed, but the Phased Array Antenna Research and Development (PAARD) team decided to purchase a second, smaller rotary table to mount directly above the existing rotary table to serve as the sample holder, and couple the existing rotary table to the third arm with an aluminum bracket. This configuration would allow the arm to be rotated directly with the rotary table, but would put a significant load on the table. To determine whether or not the load was excessive, a custom bracket was fabricated and installed and the rotation was tested. The rotary table was able to rotate the arm, but there was a noticeable jerk to the movement. The team decided to continue with the bracket and control the jerk through software acceleration and speed controls.

One major drawback to the rotary table and bracket configuration is the lack of any limit switches. While the system used to position the antenna arms is homed before every test to ensure the arms start from a known location and prevent them from being moved to a position that would run them into the end of their travel, there is no system installed to allow homing of the third arm position, or to stop the third arm before it runs into either of the other two arms. Significant damage can be

done to the rotary table should the third arm be run into one of the other arms hard enough or for long enough, possibly even damaging the rotary table beyond repair. To limit the likelihood of this happening, limits are placed in the LabVIEW control software on the range of angles that can be swept. However, these limits assume the third arm starts from the zero angle position - a position perpendicular to the plane created by the other two arms. The Velmex controller sets its zero angle position to whatever position the arm is when the controller is powered on. So, if the arm is in a position sufficiently deviant from the assumed zero angle position when the Velmex controller is powered on, and the test is run, it is still possible to run the arm into either of the other arms. Additionally, any deviation from the zero position will add error into the system measurements, since there will be a constant angular offset for every measurement. For these reasons, extra care must be taken to always ensure the third arm is at the zero angle position before running the test, and if it is not, to use the appropriate software tools to manually adjust its position and define it as the new zero angle position before running any tests. This issue could be eliminated entirely by installing limit switches at the extends of the angular sweep range, and a homing switch at the zero angle position.

3.4 Summary

This chapter covered the hardware modifications and upgrades made on the legacy anisotropic materials characterization instrument in order to allow automation of the entire calibration and materials characterization process. A second TinyG CNC

control board was added to the system to allow individual control of each antenna position, an RF switch, solid-state relay and Arduino microprocessr were added to allow automation of switching between the second and third antenna ports, and a mechanical bracket was fabricated to couple the third antenna arm to a rotary table. Each modification was discussed and complete system schematics were provided.

Chapter 4

Proposed Method for System Calibration

4.1 Introduction

The bulk of work done on this project was developing controls and a GUI using LabVIEW to streamline calibration and data collection with the instrument. These tasks could be accomplished by sending the appropriate commands to the desired device at the right time. The software development process began by developing lower-level drivers (software that handles all the particulars of performing a desired action) to abstract away the details of communicating to each device. This effectively simplified the higher level program (software that handles the flow of a desired process at a macro level), by allowing each device to be commanded to perform a desired action in a single block. The higher level program, then, could capture the logic of positioning arms, performing calibration, taking data, etc. in fewer commands. This is a common software development technique to make complex programs easier to understand. Once the higher level program was completed, the software was tested on Rogers 4350b, FR4, and an artificial dielectric (frequency selective surface) and confirmed to be working properly.

4.2 Development of Subsystem Drivers

As previously stated, software development began by writing LabVIEW drivers for each of the devices to be controlled. Each of these devices are listed below.

- Copper Mountain Planar 804/1 vector network analyzer

- Velmex B5990 rotary table (Sample holder)

- Velmex B4872 rotary table (P3 antenna arm)

- TinyG v8 CNC boards (two total)

- Mini-Circuits MTS-18XL-B RF Switch

All of these devices allow for remote control over a universal serial bus (USB) connection out of the box, except for the Mini-Circuits MTS-18XL-B RF switch, which will be controlled using the Arduino Uno Wifi Rev2 and the solid-state relay as described in chapter 3. With this custom controller, there are a total of six unique devices the computer would need to communicate with over USB. Since it is unusual for a computer to have that many physical USB ports available, a Manhattan 161039 7-port USB hub was selected to multiplex all of the devices inside the instrument's electronics box, reducing the number of physical USB ports required on the computer to two - one for the USB hub and one for the vector network analyzer (VNA). One reason this particular USB hub was selected was because it could be connected to an external power supply to allow full power transfer across all USB ports. This was not found to be needed during development, but remains an option in the future. With all devices now available for communication, the next step was to develop a means of controlling the RF Switch.

4.2.1 RF Switch Firmware

As stated in chapter 3, the RF switch could be turned on and off by applying and removing 24 VDC to its control terminals. An Arduino Uno Wifi Rev2 paired with a Crydom solid-state relay were also selected in chapter 3 to facilitate switching the 24 VDC to the switch terminals. The Arduino Uno, then, needed appropriate firmware to accept a simple command from the PC and energize or de-energize the relay in response to that command. The firmware was written using the Arduino Integrated Development Environment (IDE) to support control over a 9600 baud rate serial port. The firmware was written to accept two commands over the serial port - "switch:ON" and "switch:OFF", which turn the Arduino Uno's General Purpose Input/Output (GPIO) pin 1, the solid-state relay, and therefore the RF switch on and off, respectively. These commands are summarized in Table 4.1. With the firmware completed, the switch controller was tested using a terminal program on the development computer and the voltage applied to the RF switch was verified with a multimeter.

Command	Result
switch:ON	24VDC applied
switch:OFF	0VDC applied

Table 4.1: Commands supported by the Arduino-based RF switch controller.

4.2.2 RF Switch Driver

With the switch controller firmware completed, the LabVIEW driver could then be written. The driver code is given in Figure 4.1.
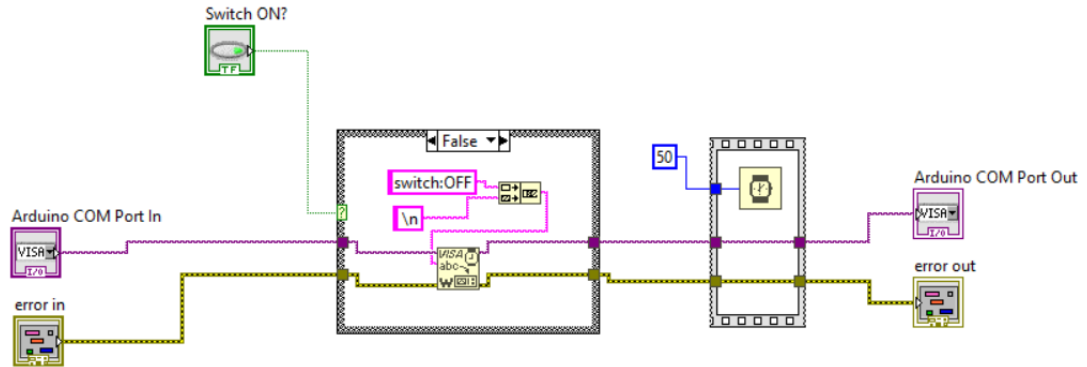
Figure 4.1: LabVIEW RF switch driver

Like all LabVIEW code, the program logic flows from the inputs (controls) to the outputs (indicators) following the wired paths. Generally, this path will be from left-to-right, as in the given driver. This program has three inputs: a boolean that specifies the desired switch position, the communication (COM) port used to communicate with the Arduino, and an error signal. The boolean input is wired to a case structure such that when the boolean is true, the command "switch:ON" is written over the COM port, and when it is false, the "switch:OFF" command is written. The "\n" appended to the end of the command is the symbol for an American Standard Code for Information Interchange (ASCII) line feed. It indicates to the Arduino that the entire command has been transmitted and is ready to be processed. Following the true/false case structure is a 50 ms delay block that pauses the program's execution for 50 ms. During testing, it was found that if multiple serial commands were transmitted in quick succession some could be skipped. This small delay ensures that that all serial operations are completed before exiting the driver.

We can see in this driver that there is no VI to open a new serial connection to the Arduino. This block would also specify the baud rate of the communication. Since multiple calls will be made to turn the switch on and off during a test, but the port should only be opened and closed once, the opening and closing of the port is left to the higher level program.

4.2.3   VNA Driver

Before beginning to write the control software for the vector network analyzer, a thorough understanding of the remote control system implemented by Copper Mountain Technologies was essential. Fortunately, this system was well documented in the "S2 and S4 series Network Analyzer COM/DCOM Programming Manual" provided on the Copper Mountain Technologies website. The manual for software version 19.1 was used during development. In addition to this manual, Copper Mountain Technologies provides LabVIEW-compatible software drivers, which were installed onto the development laptop prior to beginning software development. The drivers provided out-of-the-box access to many useful VNA features, including setup of the frequency range, number of points per sweep, etc. but many more features had to be implemented manually, which required a deeper understanding of the VNA control scheme used. The VNA uses a Standard Commands for Programmable Instruments (SCPI) interface for control. This interface essentially breaks out all VNA functions into individual commands that can be called as desired over the serial port, so long as the appropriate parameters are passed to them. The LabVIEW code provided in the drivers gave an excellent starting point for adding new SCPI commands. In fact, the

LabVIEW system was already aware of all supported SCPI commands, so the author

needed only create Virtual Instrument (VI) blocks for these commands as needed.

Table 4.2 documents all SCPI commands used in the calibration and test program,

the action they perform, any parameters they accept or data they return, and the VI

in which they are implemented.

SCPI.MMEMory.LOAD.STATe	
Description:	Recalls the specified analyzer state file. The file must be saved by the SCPI.MMEMory.STORe.STATe command.
Parameters:	File Name
VI Name:	load_state.vi
SCPI.CALCulate(Ch).PARameter(Tr).SELect	
Description:	Sets the specified trace as the active trace. Subsequent trace commands called on the active trace will then affect this trace.
Parameters:	Channel Number and Trace Number
VI Name:	set_active_trace.vi
SCPI.MMEMory.STORe.FDATa	
Description:	Saves the active trace data as a Comma Seperated Value (CSV) file.
Parameters:	None
VI Name:	save_csv.vi
SCPI.CALCulate(Ch).SELected.FORMat	
Description:	Gets or sets the format of the active trace.
Parameters:	A string corresponding to the desired format. Ex. "REAL", "IMAGinary", etc.
VI Name:	set_active_trace_format.vi
SCPI.MMEMory.STORe.STATe	
Description:	Saves the analyzer state into a file with the specified name. The state can be recalled using the SCPI.MMEMory.LOAD.STATe command.
Parameters:	File Name
VI Name:	save_state.vi
SCPI.CALCulate(Ch).PARameter(Tr).DEFine	
Description:	Gets/sets the measurement parameter of the active trace.
Parameters:	A string corresponding to the desired measurement parameter. Ex. "S_{11}, "S_{12}", "S_{21}", "S_{22}"

VI Name:	set_trace_measurement_parameter.vi
SCPI.CALCulate(Ch).PARameter(Tr).DEFine	
Description:	Gets/sets the measurement parameter of the active trace.
Parameters:	A string corresponding to the desired measurement parameter. Ex. "S_{11}, "S_{12}", "S_{21}", "S_{22}"
VI Name:	set_trace_measurement_parameter.vi
SCPI.SENSe(Ch).CORRection.COLLect.ACQuire.TRLThru	
Description:	Measures the calibration data of the thru standard.
Parameters:	None
VI Name:	TRL_Calibration.vi
SCPI.SENSe(Ch).CORRection.COLLect.ACQuire.TRLReflect	
Description:	Measures the calibration data of the reflect standard.
Parameters:	None
VI Name:	TRL_Calibration.vi
SCPI.SENSe(Ch).CORRection.COLLect.ACQuire.TRLLine	
Description:	Measures the calibration data of the line standard.
Parameters:	None
VI Name:	TRL_Calibration.vi
SCPI.SENSe(Ch).CORRection.COLLect.ACQuire.THRU	
Description:	Measures the calibration data of the thru standard.
Parameters:	None
VI Name:	TRL_Calibration.vi
SCPI.SENSe(Ch).CORRection.COLLect.SAVE	
Description:	Calculates the calibration coefficients for the set calibration type using the calibration data taken previously. Upon completion of this command, error correction is turned on.
Parameters:	Channel
VI Name:	VNA_Calibration_Save.vi
SCPI.SENSe(Ch).CORRection.COLLect.METHod.TRL2	
Description:	Sets the calibration type to two port TRL calibration and specifies which ports will be used.
Parameters:	Port 1, and Port 2
VI Name:	VNA_Calibration_Save.vi
SCPI.SENSe(Ch).CORRection.COLLect.METHod.RESPonse.THRU	
Description:	Sets the calibration type to Thru calibration and specifies which port will be the transmit and which port will be the receive.
Parameters:	The receive port, and the transmit port
VI Name:	VNA_Method_Response_Thru.vi

Table 4.2: SCPI Commands used in the LabVIEW program

As an example, the LabVIEW code for the SCPI.MMEMory.LOAD.STATe command is shown in Figure 4.2. All SCPI command VIs follow a very similar format. The VI accepts a reference to the device we are communicating with and an error line related to that reference. The SCPI block (in the center of the code) can be clicked to browse all supported VNA commands. When a particular command is selected, the block is updated with the command name and a terminal for the parameters to be wired to. For the MMEMory.LOAD.STATe command, we must pass it a string with the name and path of the file we want to load. Since the goal of these drivers is to be as generic as possible, a control is used for the "File Location" input, which allows us to pass any file location desired to the driver.
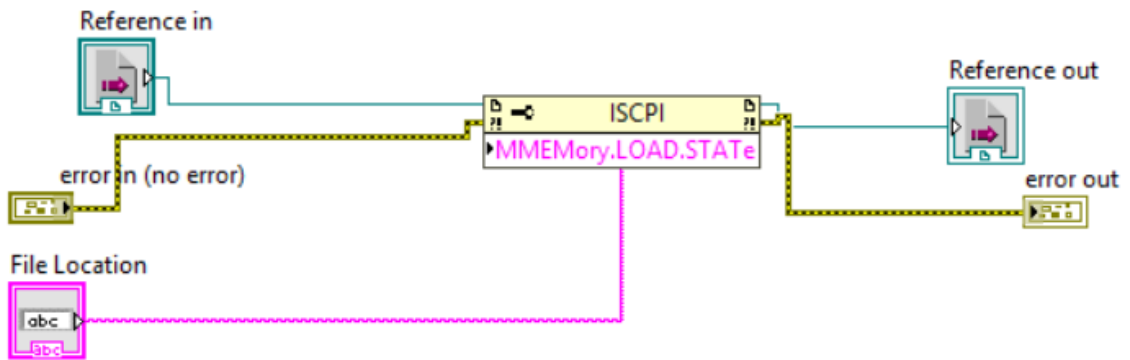

Figure 4.2: LabVIEW VNA load driver

Drivers were written for all the SCPI commands listed in Table 4.2, but they all follow the same basic format of the load driver given, so they are not discussed further here.

4.2.4 Velmex Driver

Recall from Chapter 3 that two velmex rotary tables are used, one to rotate the sample in the sample holder, and one to rotate the third antenna about the system's central axis. These motors can be controlled manually through buttons on their controllers, or through software commands sent over a serial port to the controllers. Velmex provides the "VXM Stepper Motor Controller User's Manual" on the Velmex website. This manual documents the commands supported by the controllers, the parameters they accept, and provides example controller programs. No LabVIEW-specific drivers are provided by Velmex, so the LabVIEW Virtual Instrument Software Architecture (VISA) system was used to send commands over the computer's serial port. The VISA connection is opened at 9600 baud since that is the controllers default baud rate, but that speed can be increased to a maximum of 38400 bd, if desired. Commands sent to the controller are stored in its internal memory as a complete program, which can then be run on command, rather than individual commands being run and forgotten immediately (like the SCPI protocol employed by the VNA). For this reason, every command send to the Velmex motor controller will first clear the existing program, write the new program, and then run the new program once, regardless of how simple the desired action is. The Velmex commands used are provided with a brief description in Table 4.3.

The velmex_move.vi VI, shown in Figure 4.3, was developed to command the controller to move to any absolutely indexed position relative to the motor's zero position at any desired speed. The driver accomplishes this by performing a simple

Command	Description
E	Enable On-Line mode with echo on.
C	Clear the current program memory.
R	Run the current program.
IMmAx	Move motor, m, to absolute angular position, x (in degrees).
SmMx	Set speed at of 70% motor m's power, to value, s (in steps/sec).

Table 4.3: Velmex controller supported commands.

string concatenation, inserting the desired angular position and velocity into the correct place in the command string before writing it to the controller's VISA reference. The complete program written to the Velmex controller for each movement is E, C, SmMx, IMmAx, R. The E command enables the controller's on-line mode to accept commands over the serial port, the C command clears the controller memory, the SmMx command sets the motor's speed, the IMmAx command performs the absolute move, and the R command runs the new program once. Once the command string is concatenated, it is written to the serial port using the VISA write VI. Like the switch driver, a 50 ms delay is added following the write operation to ensure the serial port is released for later code. The Velmex controllers are capable of much more complex programs including looping commands, acceleration controls, etc., but for this application only absolute position and velocity control was necessary, so that is all that was implemented.
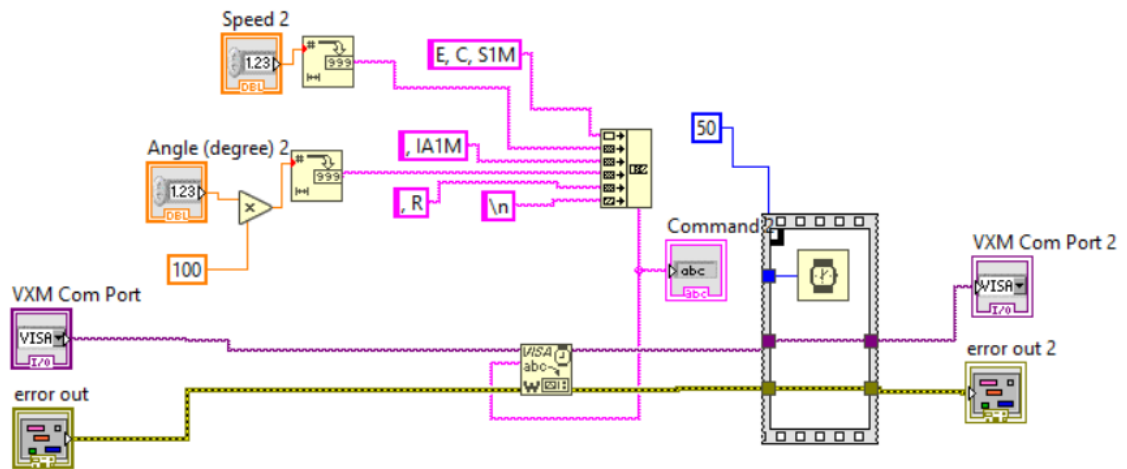
Figure 4.3: LabVIEW Velmex move driver

4.2.5 TinyG Driver

The TinyG CNC board, like the Velmex motors and the Arduino Uno, can be controlled over a VISA serial port. The Synthetos TinyG Wiki contains all the information for controlling the TinyG board over a serial connection. It is programmed to follow standard g-code commands, with some slight modifications. The TinyG_synchronous_move.vi VI was written to move each of the six axes to any position desired, accounting for the inversion of the two z-axes as described in section 2.2. Commands to home each of the axes individually, or all in a single command were also implemented in the same VI. The TinyG commands used to perform these actions are summarized in Table 4.4, and the code to send these commands is shown in Figure 4.4.

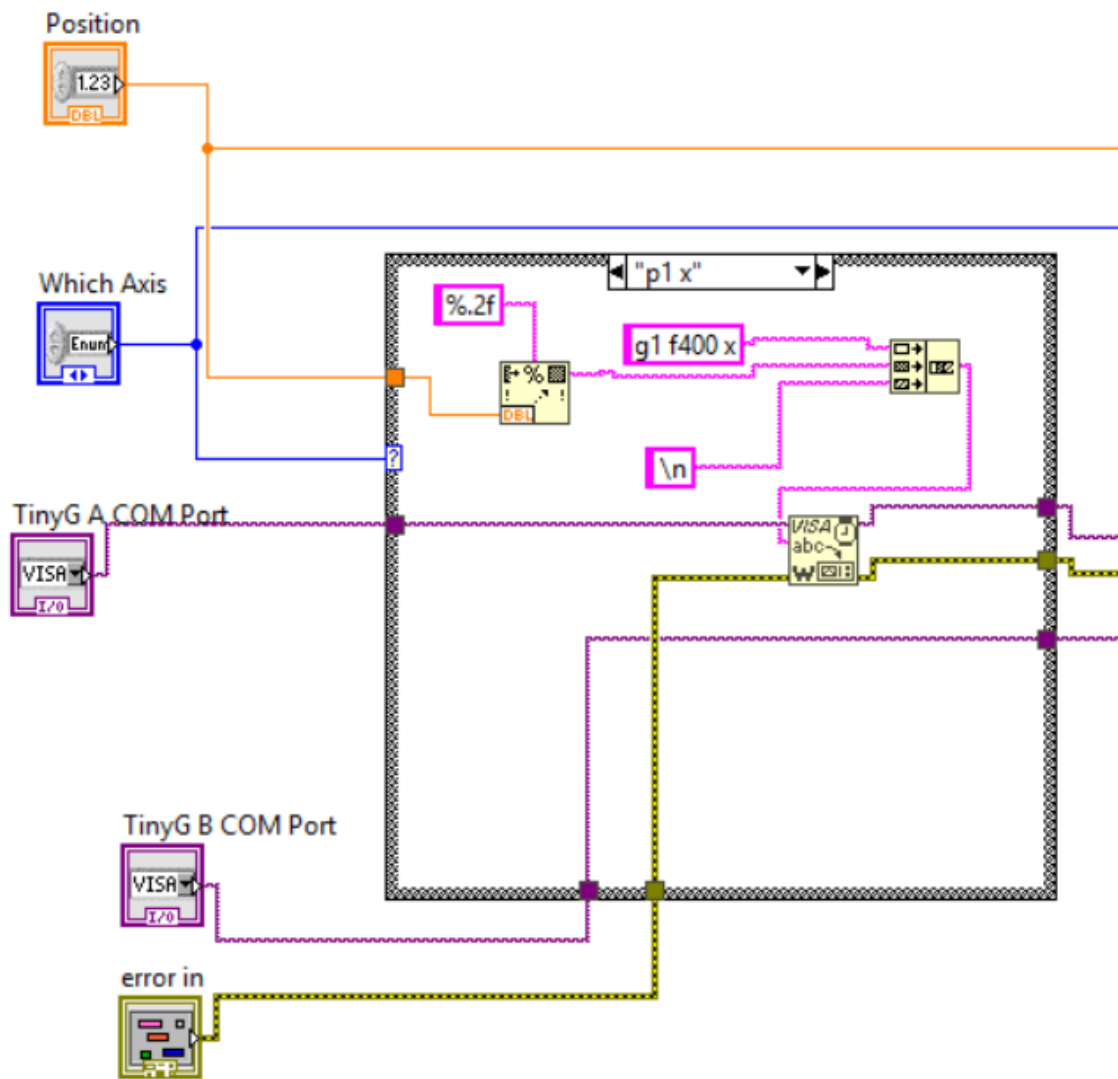| Command	Description
g1 f400 xA	Move TinyG X-axis at speed 400 mm/s to position A.
g1 f400 yA	Move TinyG Y-axis at speed 400 mm/s to position A.
g1 f400 zA	Move TinyG Z-axis at speed 400 mm/s to position A.
g28.2x	Home TinyG X-axis
g28.2y	Home TinyG Y-axis
g28.2z	Home TinyG Z-axis
g28.2xyz	Home all TinyG axes

Table 4.4: Supported TinyG Commands

Figure 4.4: LabVIEW TinyG synchronous move driver - write

The TinyG driver accepts two COM ports that correspond to the two TinyG boards used. These are not interchangeable and must be wired to the correct port. It also accepts a floating point number that corresponds to position. This number is rounded to two decimal places before being inserted into the command string. Finally, it accepts an emumerated type (enum) which is basically an unsigned integer (uint) that corresponds to a string that gives the number meaning. The enum is used to map an integer to a particular case in the case structure. The cases supported are given in Table 4.5.

Case	Description
p1 x	Move the port 1 antenna's X-axis
p1 y	Move the port 1 antenna's Y-axis
p2 x	Move the port 2 antenna's X-axis
p2 y	Move the port 2 antenna's Y-axis
p3 x	Move the port 3 antenna's X-axis
p3 y	Move the port 3 antenna's Y-axis
home p1 x	Home the port 1 antenna's X-axis
home p1 y	Home the port 1 antenna's Y-axis
home p2 x	Home the port 2 antenna's X-axis
home p2 y	Home the port 2 antenna's Y-axis
home p3 x	Home the port 3 antenna's X-axis
home p3 y	Home the port 3 antenna's Y-axis
home all	Home all 6 axes

Table 4.5: TinyG synchronous move driver - supported cases.

Each case is hard-coded to send the command to the correct COM port, either A or B, and to the correct axis. Additionally, because of the unusual axis definition used to configure the TinyG (described in Chapter 3), all commands that map to a TinyG Z-axis are inverted. This simplifies the higher-level LabVIEW code by allowing to treat all antenna axes identically, rather than having to remember to invert all commands sent to the P2 X and P2 Y axes. Once all parts of the command are concatenated

47

into a single command string, it is written to the serial port, again with a line feed character to terminate the command.

When the TinyG driver was tested, it was quickly discovered that the LabVIEW execution of the TinyG_syncrhonous_move.vi VI would complete and begin executing the next block of code as soon as a command was sent over the serial port. But, it could take a significant amount of time for the motor to move the arm to the position desired. If the drivers were left in this configuration, it could result in execution of calibration or data collection commands prior to the antennas arriving at the required positions, resulting in erroneous calibration. Some method was therefore needed to pause the LabVIEW code execution until the arm arrived at the desired location. A time-delay could be used for this purpose, but it would have to be a static time delay that works for all move commands, and would therefore be awkwardly long for short movements of the antennas. Fortunately, the TinyG board sends a response packet over the serial port once the move command is completed and the arm has arrived at the desired position. If this packet could be properly read, the LabVIEW code could be written to wait until this packet is received. To accomplish this, a loop was constructed to continually execute the VISA read command using a feedback node to concatenate the data read. This would effectively read data off of the serial port as quickly as possible and store all of the data received into a concatenated string. With all of the receive data recovered, another VI - TinyG_synchronous_read.vi - was written to search the received data on each loop iteration for the response packet corresponding to the command issued. If the response packet corresponding to the axis moved is found, the loop is exited and execution of the LabVIEW code continues.

This effectively makes the TinyG move and home commands synchronous, but in the rare case that the TinyG encounters a problem and sends an error packet instead of the expected response packet, this code will hang in the VISA read loop forever, and will have to be manually exited and the system reset. Adding support for parsing error packets and, if an error occurs, exiting the primary code operation would improve this software. The expected response packets are summarized in Table 4.6, the code to perform the VISA read loop is shown in Figure 4.5, and the code that performs the string search is shown in Figure 4.17.

Response	Description
posx:2.000,vel:0.00,stat:3	Response sent after the X-axis arrives at position 2.000.
posy:2.000,vel:0.00,stat:3	Response sent after the Y-axis arrives at position 2.000.
posz:2.000,vel:0.00,stat:3	Response sent after the Z-axis arrives at position 2.000.

Table 4.6: TinyG reponse packets
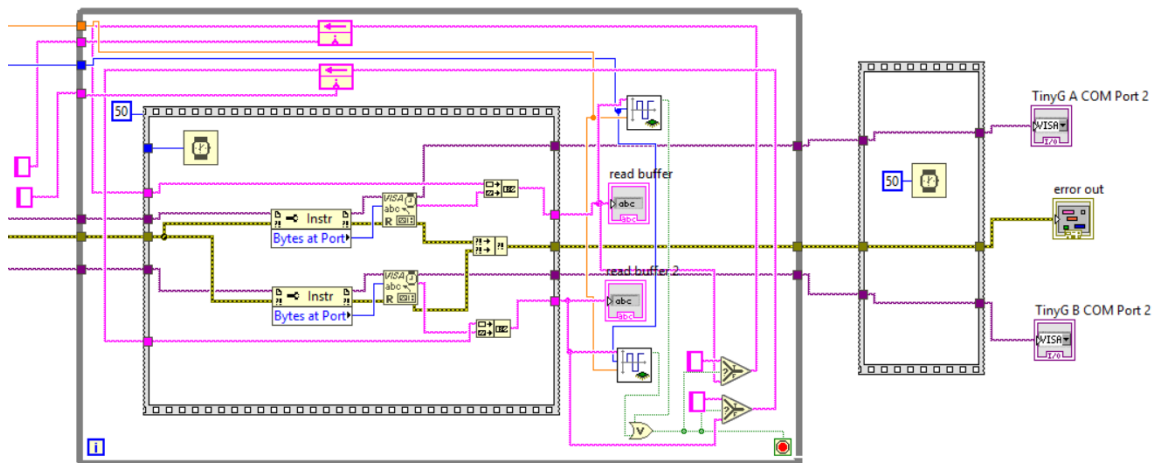
Figure 4.5: LabVIEW TinyG synchronous move driver - read loop.
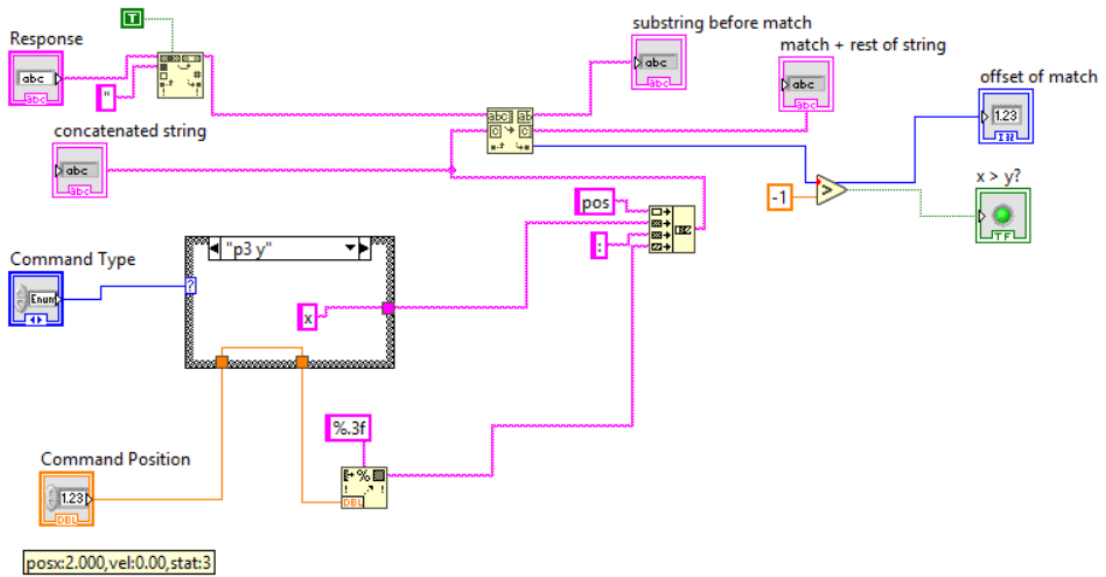
Figure 4.6: LabVIEW TinyG synchronous move driver - response parser.

4.3 Development of Automatic Calibration and Data Collection Procedure

Once all software drivers were finished, the overall calibration and data collection process could be formalized through LabVIEW code. There were two main, separate cases that needed to be supported - the broadside case and the angular sweep case. In each of these cases, the VNA needs to be calibrated to ensure accurate results. For broadside materials characterization, Transmission-Reflection-Line (TRL) calibration of the VNA was selected because of its increased accuracy, while for the angular sweep, Transmission-Reflection calibration was chosen so reduce the time required to perform the test, although TRL calibration could be used if desired for more accurate

results. The details of these two characterization processes are given in the following paragraphs.

4.3.1 Normal Incidence

For the broadside case, we must collect certain information from the user before beginning. This information is collected through the LabVIEW GUI shown in FIGURE X. The user must specify the COM ports used to communicate with the two TinyG boards and the desired x- and y-axis positions for the system to place the antennas. The program begins by homing all axes, then moving them to the user-specified positions. Once there, the thru calibration standard is collected and the position $\lambda/8$ away is calculated. A 90 degree increase in distance is the optimum point to take the line standard for TRL calibration, therefore both antennas are moved a distance of $\lambda/8$, effectively increasing the distance by $\lambda/4$. Once the new position is calculated, the antennas are moved there and the line calibration standard is taken, before returning the antennas to their previous positions. At this point the user is prompted to place the reflect calibration standard into the sample holder. Once the user clicks the "OK" button on the screen, confirming the reflect standard is in place, the reflect calibration is run and system calibration is completed. At this point, the VNA is set to have four traces display: S_{11}, S_{12}, S_{21}, and S_{22}, all as log-magnitude. Time gating is than applied to each trace using a 100 ns window. Once time gating is applied, the traces are reconfigured to display S_{11} real, S_{11} imaginary, S_{21} real, and S_{21} imaginary, respectively. With time gating applied and the traces properly configured, the user is then prompted to remove the reflect standard and insert the sample into the sample

holder. Once they click the "OK" button confirming the sample is in the sample holder, the VNA data for all four traces is saved into the /CSV directory, and the Smith_algorithm.m Matlab script is called to process the data. Once the script finishes running, its results are displayed in the LabVIEW GUI and the program finishes execution. This process is summarized in the flowchart given in Figure 4.7.

4.3.2 Oblique Incidence

For the oblique incidence case, the program performs the same initialization procedures as the broadside case: opening all the serial ports, homing the antennas, and moving the antennas to their starting positions. In addition to these tasks, for the oblique case, the software also performs validation of the user-entered data for the angular sweep to be performed. If the data would run the arm into the rest of the system, testing is aborted and an error message is displayed. Once initialization is completed and the antennas are positioned, the RF switch is set to so that the P1 and P2 antennas are connected to the VNA and Thru calibration is performed to calibrate the system's S_{21} measurement. This calibration data is then saved to the instrument's computer as the broadside_calibration.sta state file. Next, the user is prompted to insert the reflect standard into the sample holder. Once they confirm the standard is in place, the S_{11} calibration sweep is performed.

The first step in the S_{11} calibration sweep is to change the state of the RF switch so that the P1 and P3 antennas are now connected to the VNA. Next, the P3 antenna arm and sample holder are rotated to their starting positions. Just like in the case of the TinyG driver, execution of the LabVIEW code continues as soon as the move
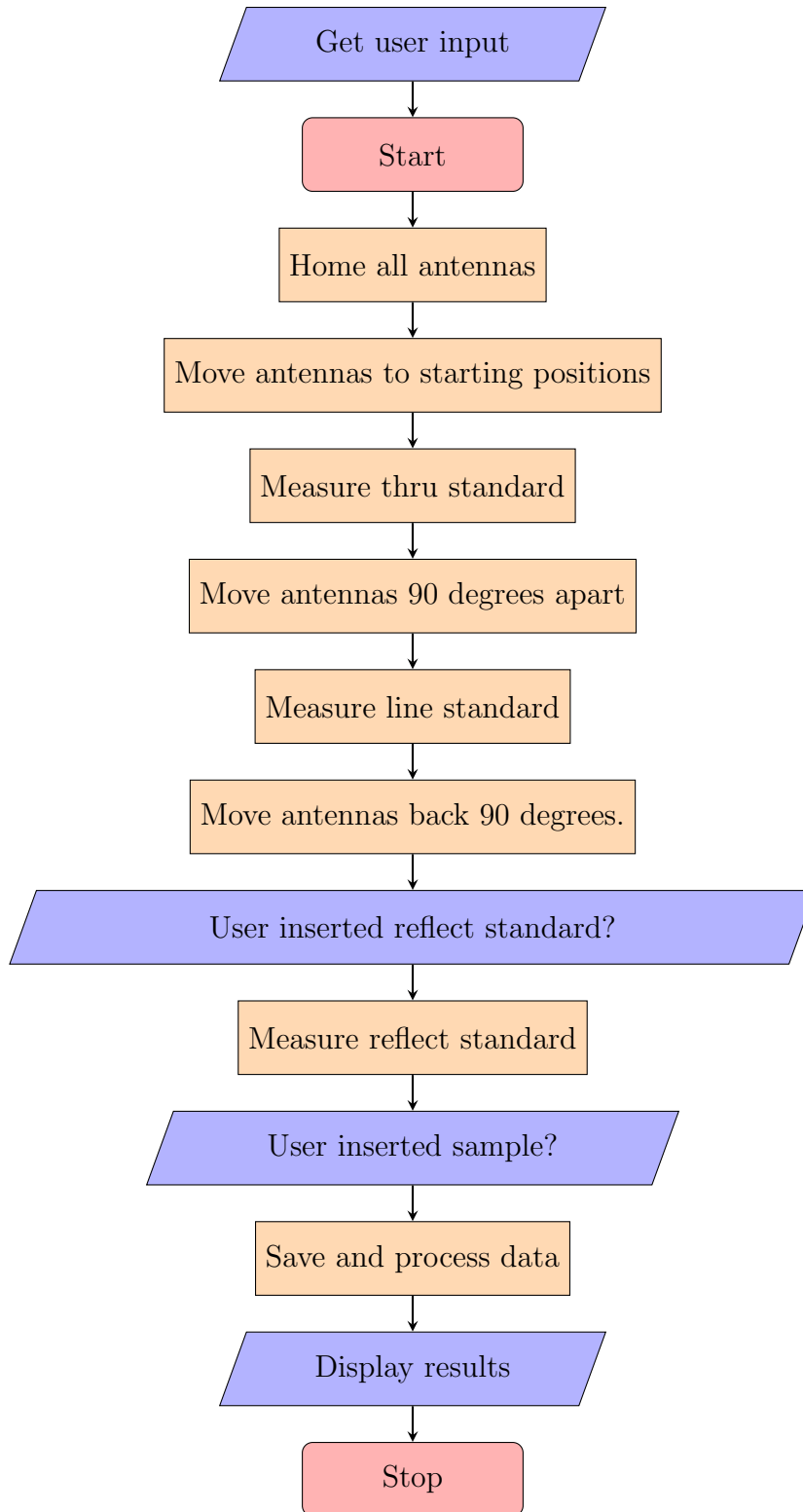
Figure 4.7: Flow chart of normal incidence logic

command is issued rather than once the tables arrive as the desired position. To prevent this, the program manually calculates the angular distance both rotary tables must move, and divides it by the speed the table moves at, accounting for the different gearing of the two tables. The program is then delayed for this calculated time, and once the time expires, execution of the LabVIEW code continues. With the tables now at the appropriate position, Thru calibration is once again performed on the VNA's S_{21} measurement, although because of the antenna configuration, this is now calibrating to measure the sample's S_{11} value. This calibration is then saved to the anisotropic_calibration_state_XX.sta file, where XX is a number that corresponds to the angle of incidence the calibration was taken at. Once the calibration state is saved, the next angle in the sweep is calculated, and the entire process is repeated for the next angle. In this way, the sample and P3 antenna arm are swept through the entire angular range and Thru calibration is performed at every test angle. Once the calibration is completed, the P3 antenna arm and the sample return to their original positions and testing of the sample can begin.

After the rotary tables have returned to their original positions, the user is prompted to insert the sample into the sample holder. Once they click the "Ok" button, indicating that the sample is ready, the sample and P3 antenna arm are rotated to their starting positions, just like in the calibration phase. Once the rotary tables have arrived, the RF switch is set to measure between P1 and P2, the broadside_calibration.sta state file is loaded, time gating is configured on the VNA channel traces, and the data is saved to the anisotropic_data_S21_XX.csv file, where XX is a number which corresponds to the tested angle of incidence. With the S_{21}

data saved, the RF switch is toggled to measure between the P1 and P3 antennas, the anisotropic_calibrationi_state_XX.sta state file corresponding to the current angle of incidence is loaded, time gating is configured on the traces, and the data is saved to the anisotropic_data_S11_XX.csv file. Again, the XX corresponds to the current angle of incidence. At this point, we have measured both the S_{21} and S_{11} values for the sample at the the given angle of incidence, so the sample holder and P3 antenna arm are rotated to the next angular position and the entire process is repeated. This continues until testing has been performed at every angular position, after which the rotary tables are returned to their starting positions, and the data is passed to a Matlab script for processing. Once processing is completed, the data is displayed in the LabVIEW GUI. The high-level flowchart of this process is given in Figure 4.8.

4.4 Extraction Algorithm Improvements

The Nicholson-Ross-Weir (NRW) algorithm and the Smith algorithm were previously used to extract the permeability and permittivity from the measured S-parameters [14]. These methods are convenient, since they can be computed directly from the S-parameters, but were resulting in large inaccuracies in the computed permeability and permittivity. One weakness of this method is its sensitivity to differences in the position of the reflect standard and the sample. This error is embedded into the S_{11} measured values, and can be corrected by applying a phase shift to S_{11} if the offset is known. If the offset is not known, but both S_{12} and S_{22} are also measured, a four parameter method can be used to eliminate this error, since the phase offset added
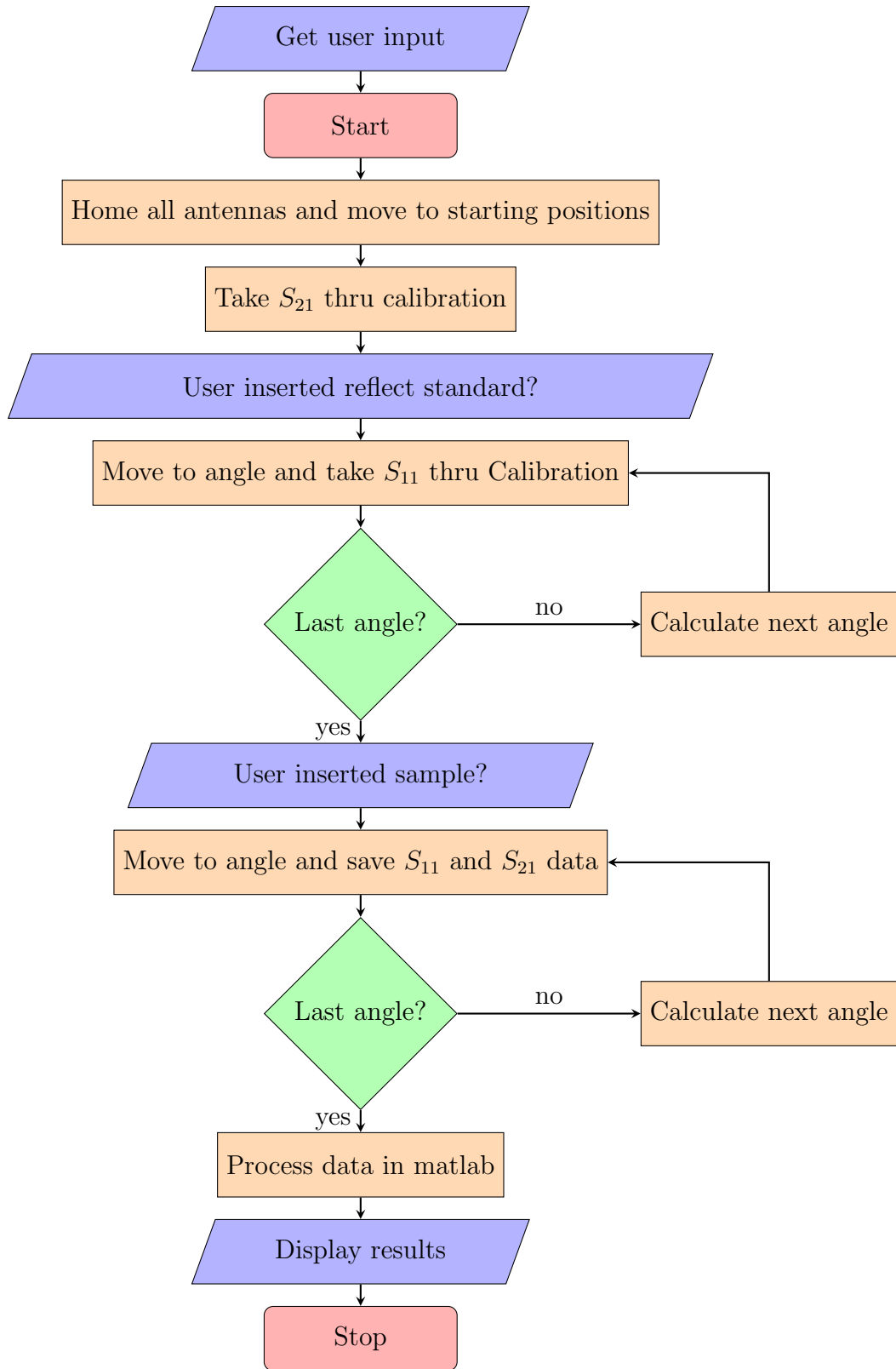
Figure 4.8: Flow chart of oblique incidence logic

to S_{11} will be effectively subtracted from S_{22}. However, the four-parameter method is an iterative technique, and therefore cannot be directly computed. Schultz gives an example of the four-parameter method in "Focused Beam Methods" using Newton's Method as the numerical convergence technique to solve for permeability and permittivity [4], but Newton's Method requires an accurate initial guess to converge. The algorithm as given in "Focused Beam Methods" was implemented in Matlab, but failed to converge for the test data and initial guesses provided (the theoretical values of permeability and permittivity for the known materials were used as guesses). Because Newton's Method failed to converge, an alternative numerical technique was needed. Due to time constraints, a brute-force method was employed instead of finding a a more appropriate numerical convergence technique. The brute force method provided preliminary results quickly, and can be replaced with a more elegant solution at a later time. The technique is described below.

There are two equations relating reflectivity and transmissivity to S_{11} and S_{21}. They are given below [4].

$$S_{11} = \frac{\Gamma(1 - T^2)}{1 - \Gamma^2 T^2} \tag{4.1}$$

$$S_{21} = \frac{T(1 - \Gamma^2)}{1 - \Gamma^2 T^2} \tag{4.2}$$

We can then relate reflectivity and transmissivity to the permeability and permittivity with the following general formulas [4].

$$\Gamma_{TE} = \frac{\mu\cos\theta - \sqrt{\mu\epsilon - \sin^2\theta}}{\mu\cos\theta + \sqrt{\mu\epsilon - \sin^2\theta}} \tag{4.3}$$

$$\Gamma_{TM} = \frac{\sqrt{\mu\epsilon - \sin^2\theta} - \epsilon\cos\theta}{\sqrt{\mu\epsilon - \sin^2\theta} + \epsilon\cos\theta} \tag{4.4}$$

$$T = e^{-ik_0 t\sqrt{\mu\epsilon - \sin^2\theta}} \tag{4.5}$$

These general forms of the equations are used to calculate permeability and permittivity versus incident angle, but for the normal incidence case, they simplify to the following.

$$\Gamma = \frac{\sqrt{\frac{\mu}{\epsilon}} - 1}{\sqrt{\frac{\mu}{\epsilon}} + 1} \tag{4.6}$$

$$T = e^{-ik_0 t\sqrt{\mu\epsilon}} \tag{4.7}$$

These simplified forms of the equations are used to calculate permeability and permittivity in the broadside configuration. For the specific case of FR4 tested in the broadside configuration, the permeability is also known to be one. If we make the assumption that a material's permeability is a given value, we reduce the number of unknowns we need to solve for and therefore reduce the number of equations we need to solve. This allows us to eliminate the S_{11} equation entirely, thereby removing all error embedded in the measured S_{11} value. In this case, the reflectivity equation simplifies to the following.

$$\Gamma = \frac{\sqrt{\frac{1}{\epsilon}} - 1}{\sqrt{\frac{1}{\epsilon}} + 1} \tag{4.8}$$

Finally, if only S_{11} and S_{21} are measured, then the extracted constitutive parameters will be very sensitive to the sample's position, with any deviation in position from the exact center between the two antennas manifesting as a phase error in S_{11}.

4.5 Results

The results obtained using the developed LabVIEW software and the Matlab script for both the normal, and the oblique incidence cases are given below. Rogers 4350b, FR4, and an anisotropic dielectric (frequency-selective surface) were tested.

4.5.1 Normal Incidence

Rogers 4350b was selected to verify the system's calibration because of its very tightly controlled dielectric constant and loss tangent.
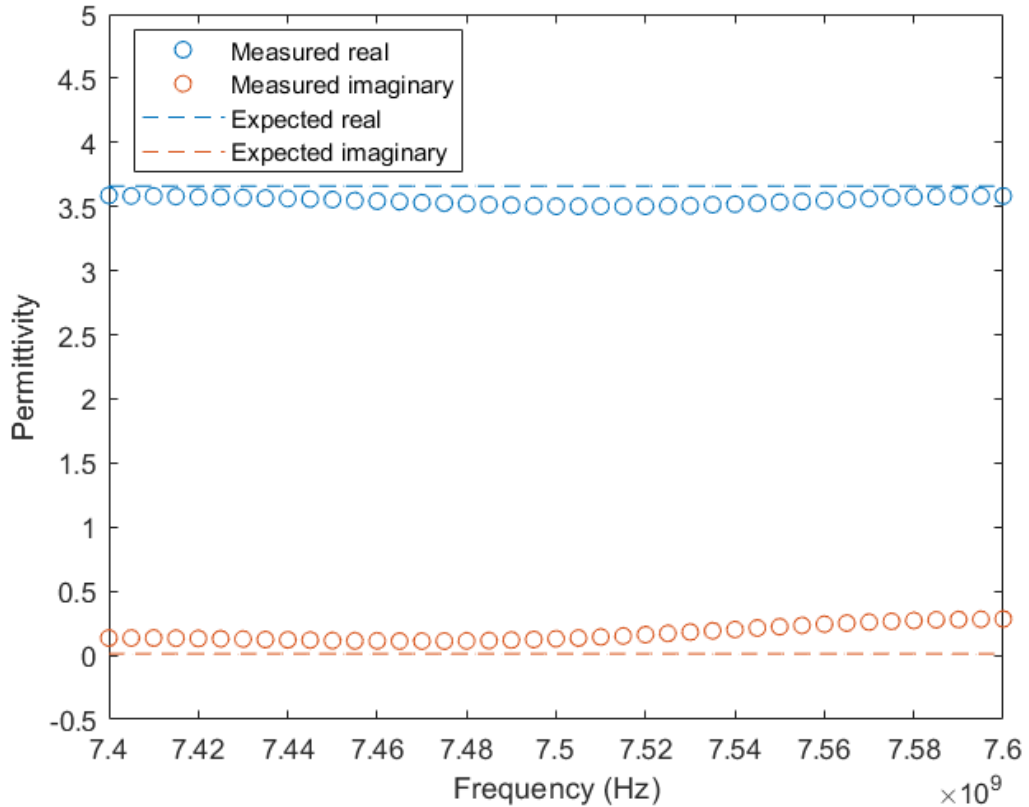
Figure 4.9: Rogers 4350b permittivity measured at normal incidence. [3]

We can see that at normal incidence, across the frequency band, the measured imaginary permittivity deviates from the expected range by a maximum of 0.2833. This occurs towards the upper end of the frequency range, while the middle to lower range falls much closer to the expected value. At this time, the largest source of error is from the polyrod antennas. As previously stated, these antennas produce a quasi-constant phase front, but any deviation in phase across the beam that strikes the sample introduces error in the system. Additionally, the beam produced by these antennas has a diameter of approximately 6 in at the distance used, as shown in Figure 4.24. Since the system does not presently use a frame to hold the sample materials, deflection can occur across the sample surface and introduce additional errors into the

measurement. The sample thickness is also not perfect, and is determined by taking several measurements and averaging them. Non-uniform sample thickness introduces errors into the measurement and makes it difficult to manually correct the phase offset in S_{21}, since it is based on a constant sample thickness.
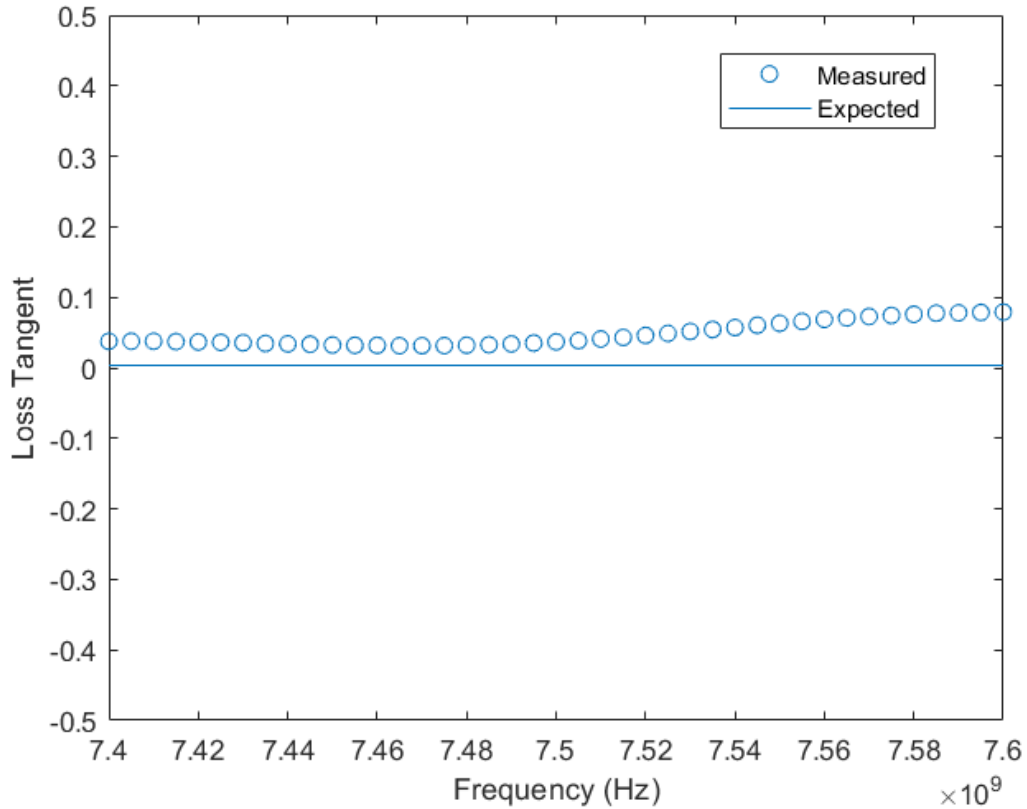
Figure 4.10: Rogers 4350b loss tangent measured at normal incidence. [3]

The loss tangent measurement is calculated from the permittivity measurement, and therefore also has less accurate results towards the upper end of the frequency band. Because the loss tangent of Rogers 4350b is so low (0.0034), it requires an extremely accurate measurement of permittivity to produce an accurate result. For example, ± 0.05 is the tolerance on the permittivity specified by Rogers Corporation.

To achieve the loss tangent specified by Rogers Corporation of 0.0034, assuming a constant real permittivity of 3.66, the imaginary part of permittivity must be 0.012444, since loss tangent is calculated as the imaginary part of permittivity divided by the real part. Adding or subtracting the 0.05 tolerance to the imaginary part of the permittivity while holding the real part constant creates a range of possible loss tangents from -0.0103 to 0.1706. This relatively small error in the permittivity measurement has become a large error in the loss tangent. This simple analysis shows that a system must be able to measure the imaginary part of permittivity extremely accurately in order to measure even a moderately accurate loss tangent [3].
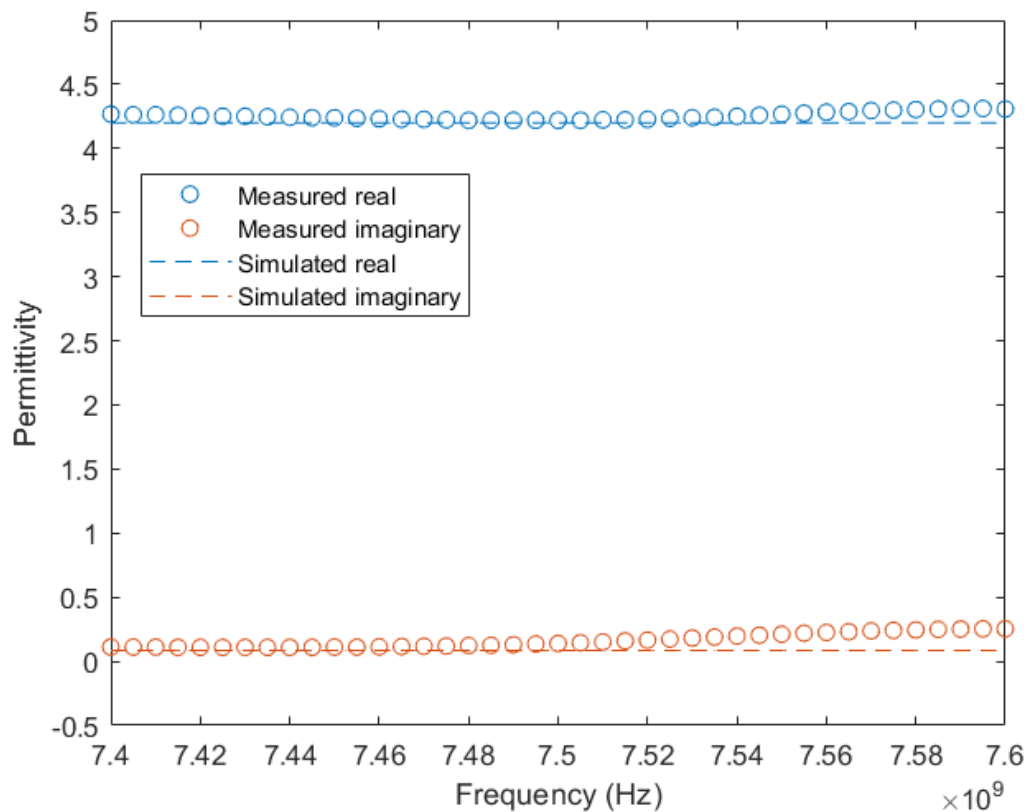

Figure 4.11: FR4 permittivity measured at normal incidence.

Figure 4.11 shows the measured permittivity of FR4 versus the simulated permittivity (of 4.2). We can see that the measured permittivity only deviates from the simulated by approximately 0.05, but since the permittivity of FR4 is not very tightly controlled, and can generally fall anywhere between 4-4.7 the simulated value may not correspond very closely to this particular sample.
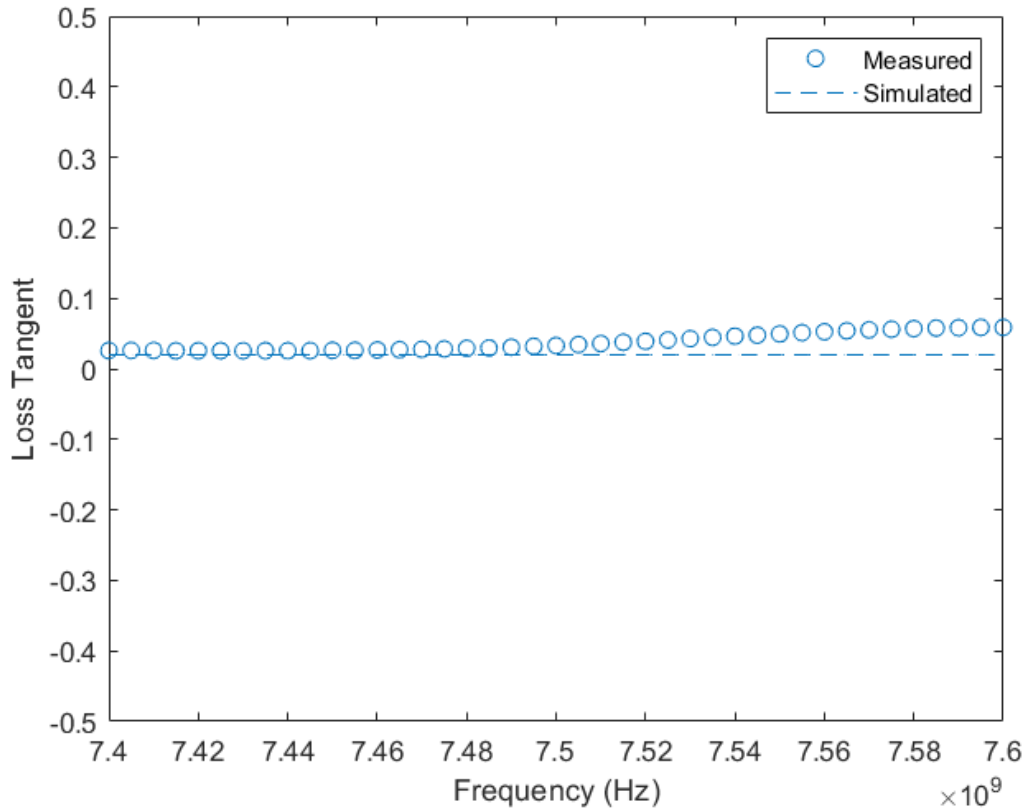
Figure 4.12: FR4 loss tangent measured at normal incidence.

Figure 4.12 is the loss tangent measurement for the permittivity measurement previously shown. As with Rogers 4350b, loss tangent requires extremely accurate permittivity measurements to be accurate. Again, we see that the measurements are more accurate at the lower end of the frequency range tested than the upper end, likely due to the polyrod antenna behavior discussed later in this chapter.

4.5.2 Oblique Incidence

The results obtained using the developed LabVIEW software and the Matlab script for the case of oblique incidence are given below.
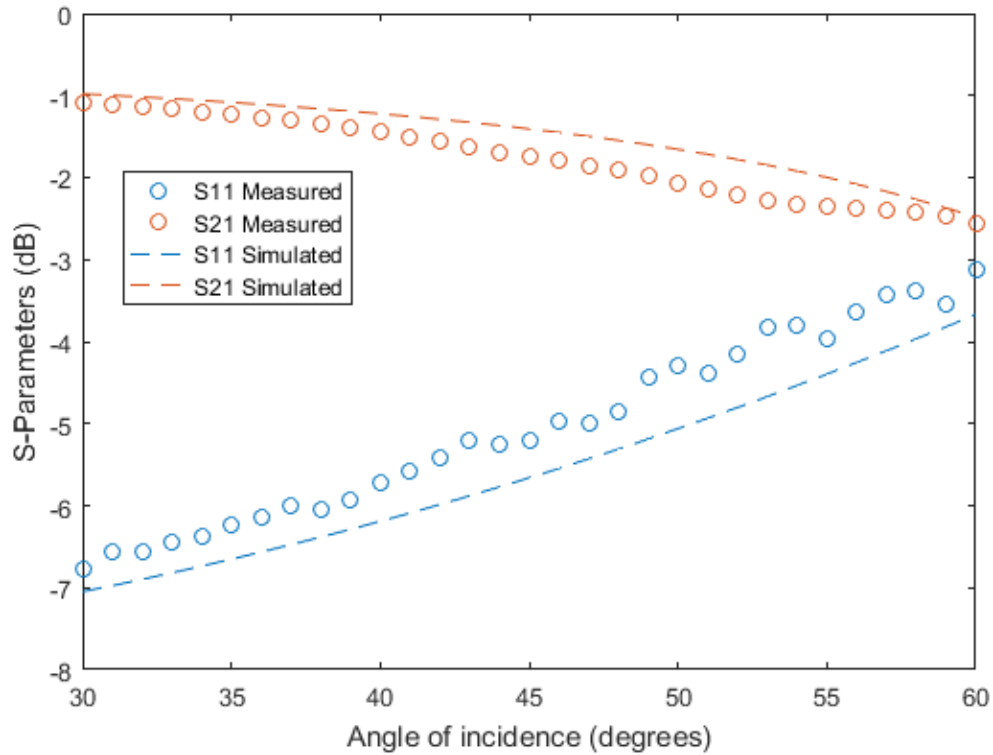
Figure 4.13: Rogers 4350b S-parameters measured at oblique incidence.

Figure 4.13 shows the magnitude of the measured S-parameters compared to the simulated S-parameters for Rogers 4350b. We can see that our error increases at greater angles of incidence. This appears to be caused by the reduced effective sample width due to the projection of the rotated sample onto the antenna plane. Since the antenna beam is fairly large ($\sim$6 in diameter) at the distance tested, the minimum sample size should be 9 in by 9 in. At an incident angle of 60 degrees, the sample width is reduced by half. Since the samples are not 18 in wide, significant

errors are introduced into our results by edge effects, and direct transmission between the P1 and P2 antennas at the larger incident angles. Over the course of the test, as the sample rotates and its effective width shrinks, the antenna beam begins to diffract at the edges of the sample, causing ripples in the measured S_{11} and S_{21} values. Eventually, the effective sample width shrinks enough that a portion of the antenna beam is able to transmit directly to the receive antenna, resulting in a sharp increase in the magnitude of the measured S_{21}, but a significant added phase error. This phase error is reflected in the calculated permittivity in Figure 4.14. Increasing the sample size would eliminate errors from edge effects and direct transmission, but would introduce larger errors from sample deflection as well as increasing the cost to test a material.
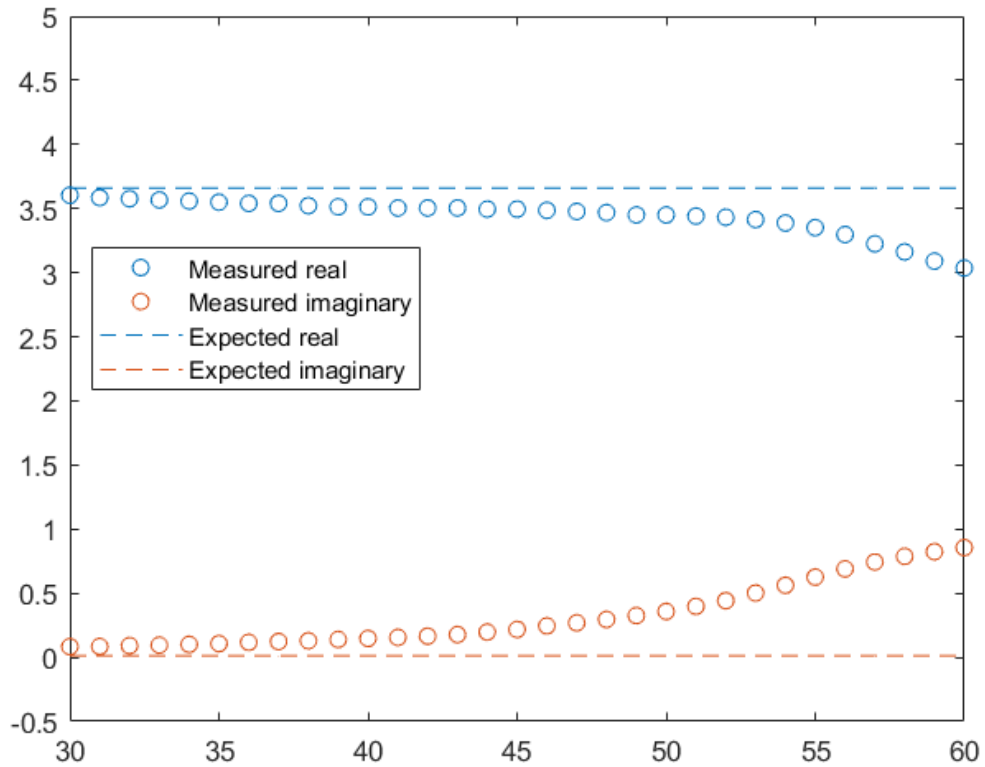
Figure 4.14: Rogers 4350b permittivity measured at oblique incidence. [3]

Figure 4.14 shows the measured real and imaginary permittivity for Rogers 4350b along with the expected values from the Rogers Corporation datasheet. We can see that we achieve highest accuracy at the lower incident angles, and the lowest accuracy at the greatest incident angles. As discussed on the previous plot, the magnitude and phase of the measured S_{21} are affected by diffraction fields as the sample's effective width is reduced, but the largest errors occur at the very end of the scan range. Recall that the magnitude of S_{21} was quite accurate at the 60 degree incident angle, but this was due to direct transmission between the P1 and P2 increasing the measured magnitude. Direct transmission causes large phase errors to be introduced since a portion of the received fields are no longer traveling through the dielectric at all.
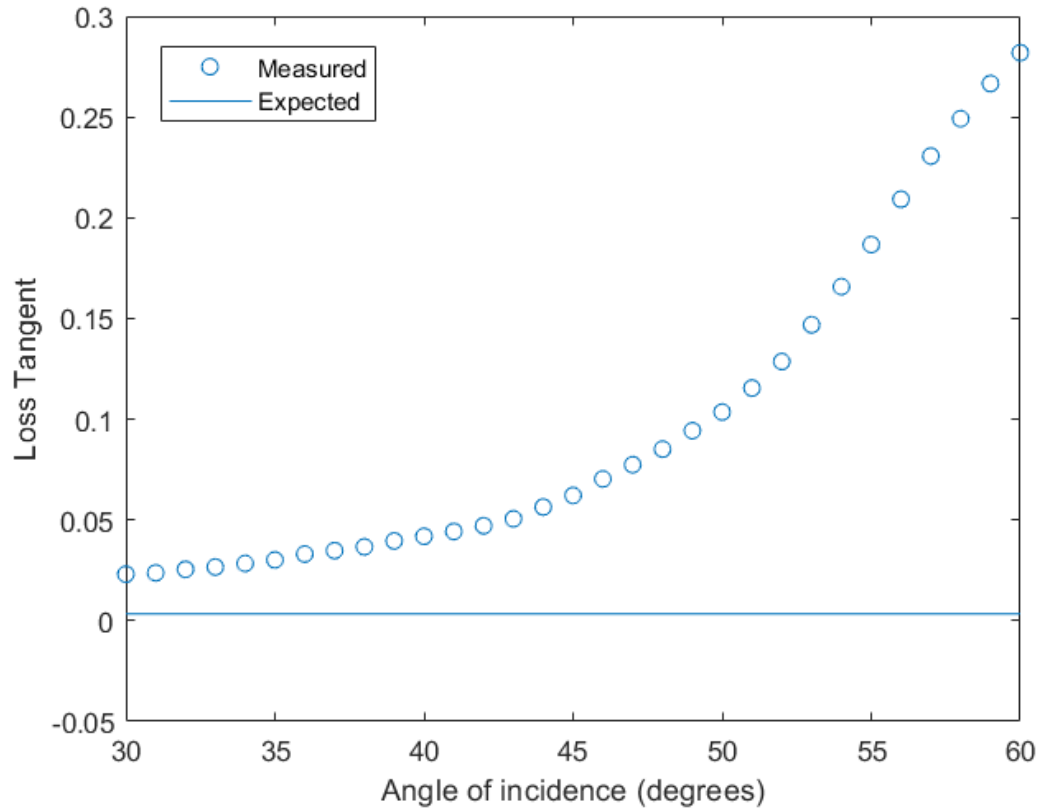
Figure 4.15: Rogers 4350b loss tangent measured at oblique incidence. [3]

The loss tangent for Rogers 4350b was also calculated across incident angle, as shown in Figure 4.15. As previously stated, errors are introduced into this data because of the edge diffraction and direct transmission occurring at the larger angles of incidence. Besides these errors, the system itself is less accurate measuring at oblique angles of incidence than at normal incidence because of the use of TR calibration instead of TRL calibration, as stated in Chapter 2.
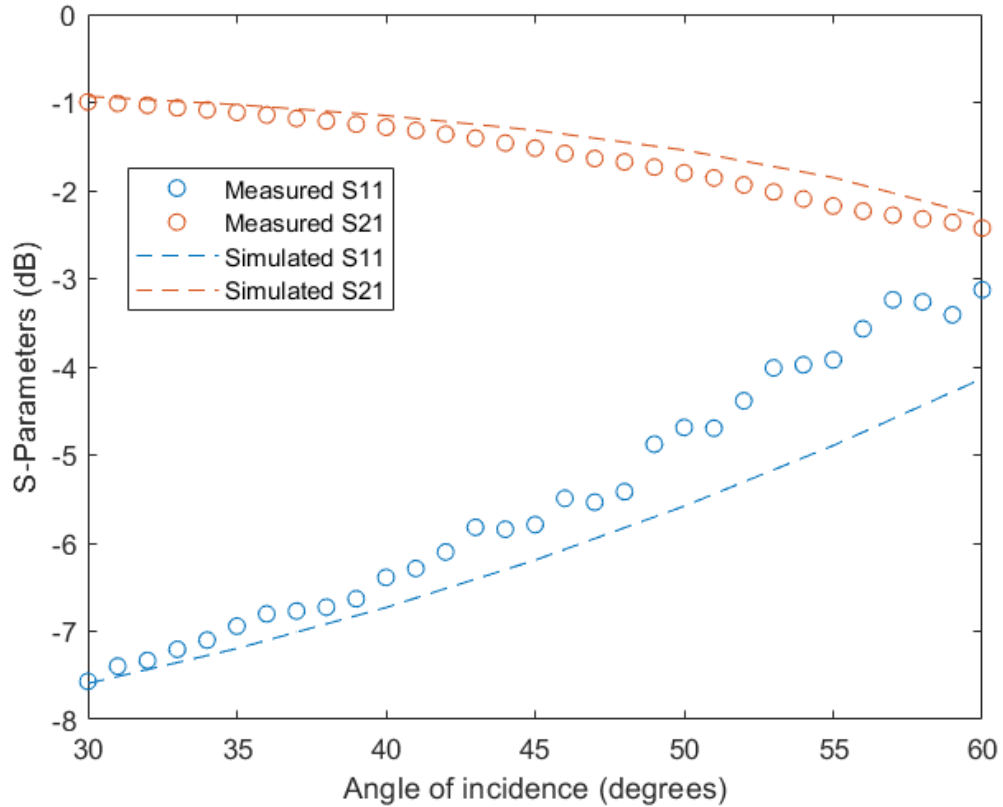
Figure 4.16: FR4 S-parameters measured at oblique incidence.

FR4 was also tested at oblique incidence, and the measured S-parameters compared to the simulated parameters. The S_{21} values are close to the simulated values, deviating by a maximum of 0.35 dB, but the S_{11} values are worse, deviating by up to 1.35 dB in some places. Interestingly, the error in the measured S_{11} value increases significantly more than the measured S_{21}. As stated previously, this increase in error is likely due to the edge effects introduced by the drop in effective sample width at larger angles of incidence. It is difficult to predict how the antenna beam diffracts under these kinds of conditions, but it appears to be reducing the accuracy in S_{11} more than S_{21}.
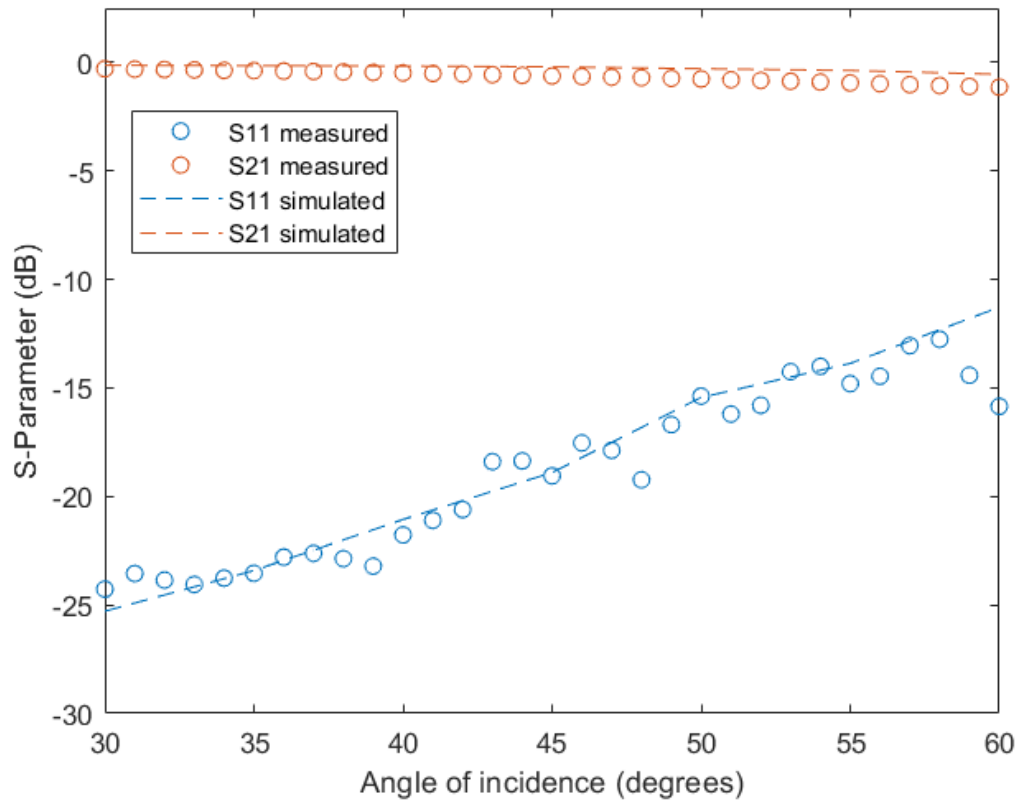
Figure 4.17: Artificial dielectric S-parameters measured at oblique incidence.

Finally, an artificial dielectric was tested at oblique incidence. Here, the measured S_{21} and S_{11} are both less accurate than for FR4, with S_{21} deviating from the simulation by 0.53 dB max, and S_{11} deviating by 4.57 dB at its maximum point, but less than 2 dB for most incident angles. In this plot, S_{11} measurements do not appear to have any pattern for being overestimated or underestimated, but instead fluctuate about the expected values. Since the artificial dielectric is narrower than the FR4 sample, it appears that the edge effects begin taking place prior to the initial 30 degree rotation.

4.5.3 Quantification of Errors

The errors for Rogers 4350b and FR4 at normal incidence, and Rogers 4350b at oblique incidence, are given in Table 4.7. The maximum, minimum, and mean errors are given in absolute deviation from the desired values for each. We can see that the errors for FR4 and Rogers 4350b are both fairly low at normal incidence, with slightly higher errors in the imaginary measurements than the real measurements. The errors are worse at oblique angles of incidence, but as previously discussed, this is due to edge diffraction and direct transmission errors introduced at increasing angles of incidence.

Rogers 4350b - normal incidence	
Real permittivity minimum error:	0.0734
Real permittivity maximum error:	0.1575
Real permittivity mean error:	0.1155
Imaginary permittivity minimum error:	0.0987
Imaginary permittivity maximum error:	0.2709
Imaginary permittivity mean error:	0.1578
FR4 - normal incidence	
Real permittivity minimum error:	0.0192
Real permittivity maximum error:	0.1113
Real permittivity mean error:	0.0534
Imaginary permittivity minimum error:	0.0251
Imaginary permittivity maximum error:	0.1693
Imaginary permittivity mean error:	0.0774
Rogers 4350b - oblique incidence	
Real permittivity minimum error:	0.0564
Real permittivity maximum error:	0.6240
Real permittivity mean error:	0.2165
Imaginary permittivity minimum error:	0.0707
Imaginary permittivity maximum error:	0.8435
Imaginary permittivity mean error:	0.3118

Table 4.7: Permittivity absolute error.

4.5.4 Analysis of Polyrod Antennas

After analyzing the data, it was determined that the polyrod antennas were a major source of measurement error at this time. Figure 4.20 shows the return loss for the polyrod antennas is less than -10 dB for only a small region around 7.5 GHz (over the 7-8 GHz band that the VNA is capable of). If the proposed RF scanner is running at a frequency outside of this small range, the antenna will create significant errors in the system [2] [30] [31] [32]. The SAQ-103039-90-S1 spot-focusing lens antenna from Sage Millimeter, Inc. was selected as a potential replacement for the polyrod antennas. It is a horn antenna equipped with a dielectric lens to focus the beam. It's return loss is shown in Figure 4.21.
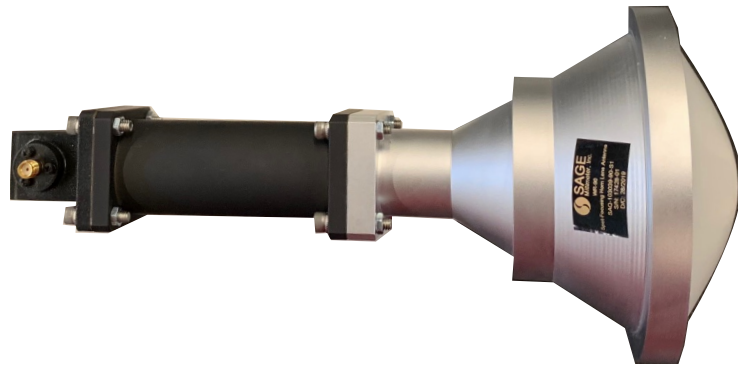
Figure 4.18: SAQ-103039-90-S1 spot-focusing lens antenna.

Figure 4.19: Polyrod antenna.
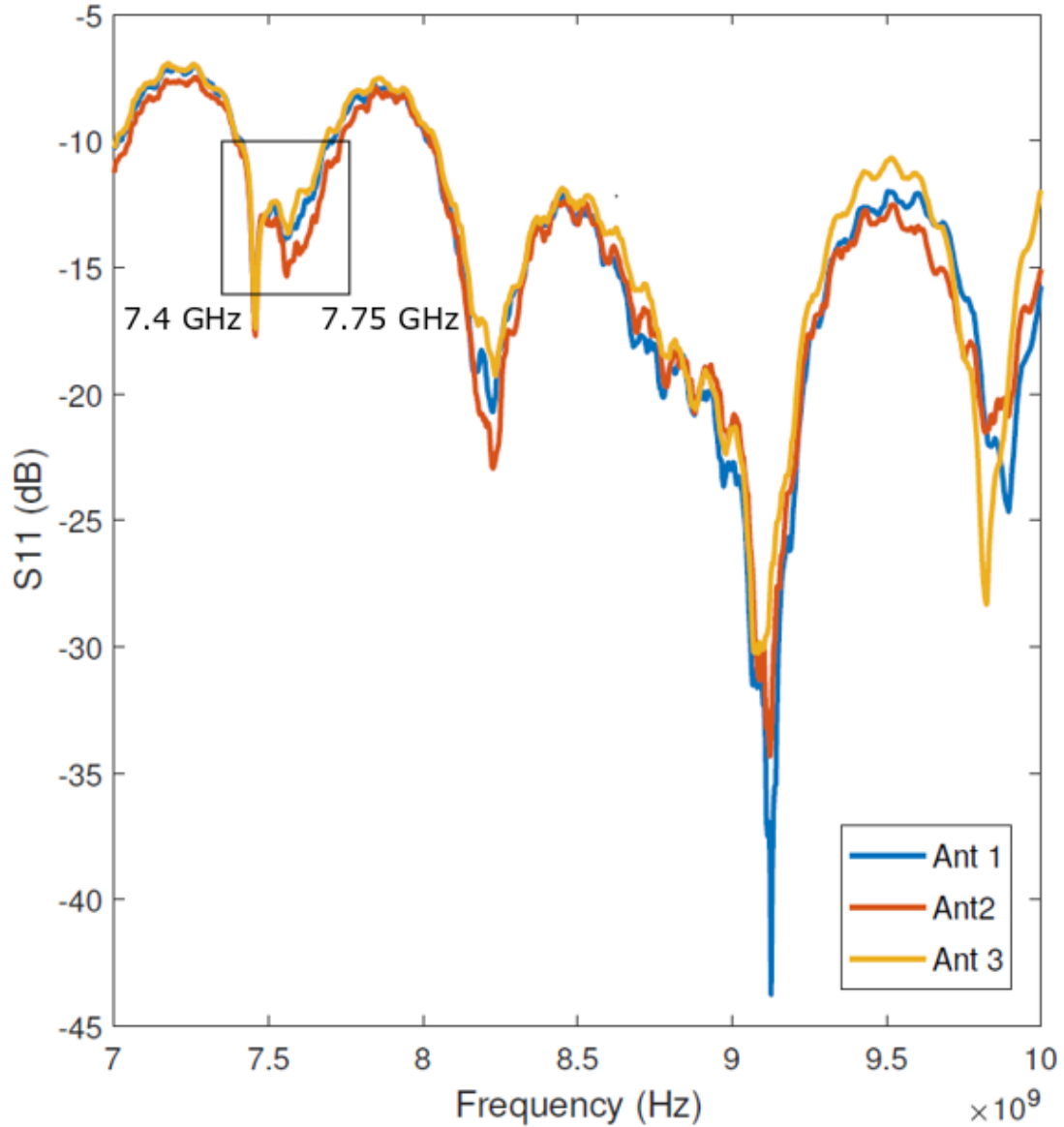
Figure 4.20: Polyrod antenna S_{11} versus frequency.

According to its datasheet, the SAQ-103039-90-S1 focused-beam antenna operates from 9.5-10.5 GHz. From the plot of the antenna's return loss shown in Figure 4.21, we can see that is is less than -15 dB in operating region, and less than -20 dB at the center frequency of 10 GHz. This is a good frequency response, and is better response than the polyrod antennas.
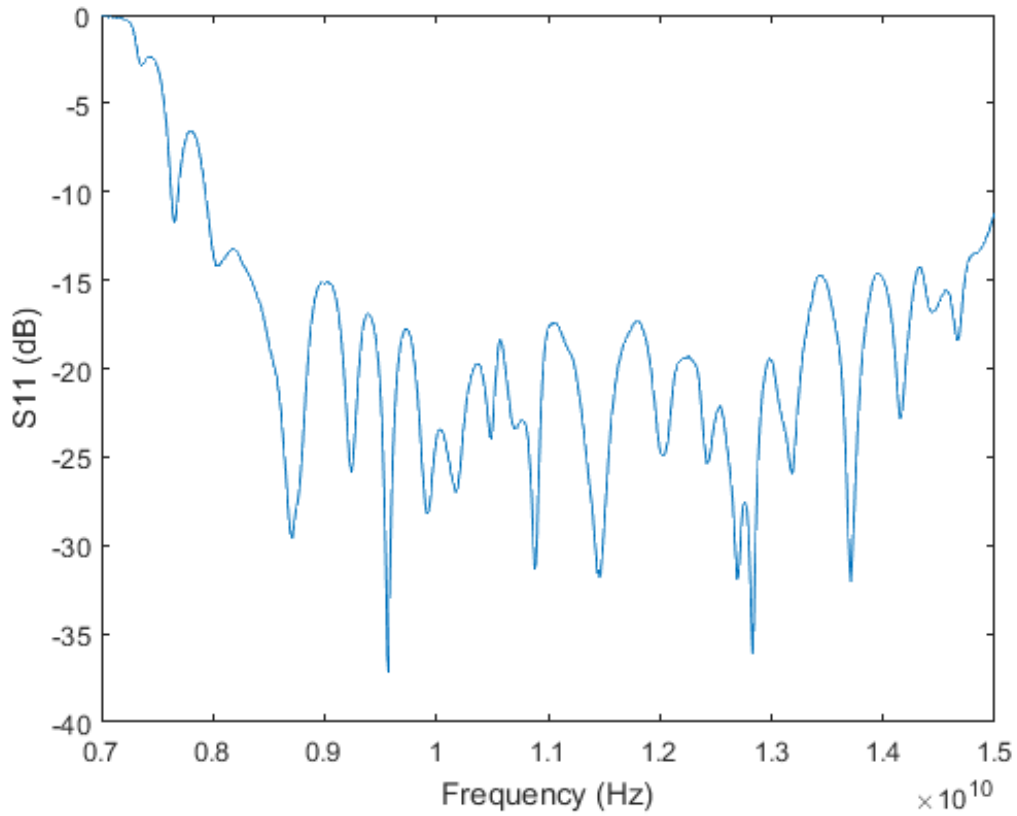
Figure 4.21: SAQ-103039-90-S1 spot-focusing lens antenna return loss.

To better understand the antenna behaviors, both were tested in the near field chamber and compared to both a standard WR-90 waveguide. The waveguide and the polyrod antenna were tested at 7.5 GHz, but since the focused-beam antenna only operates from 9.5-10.5 GHz, it was tested at 10 GHz.
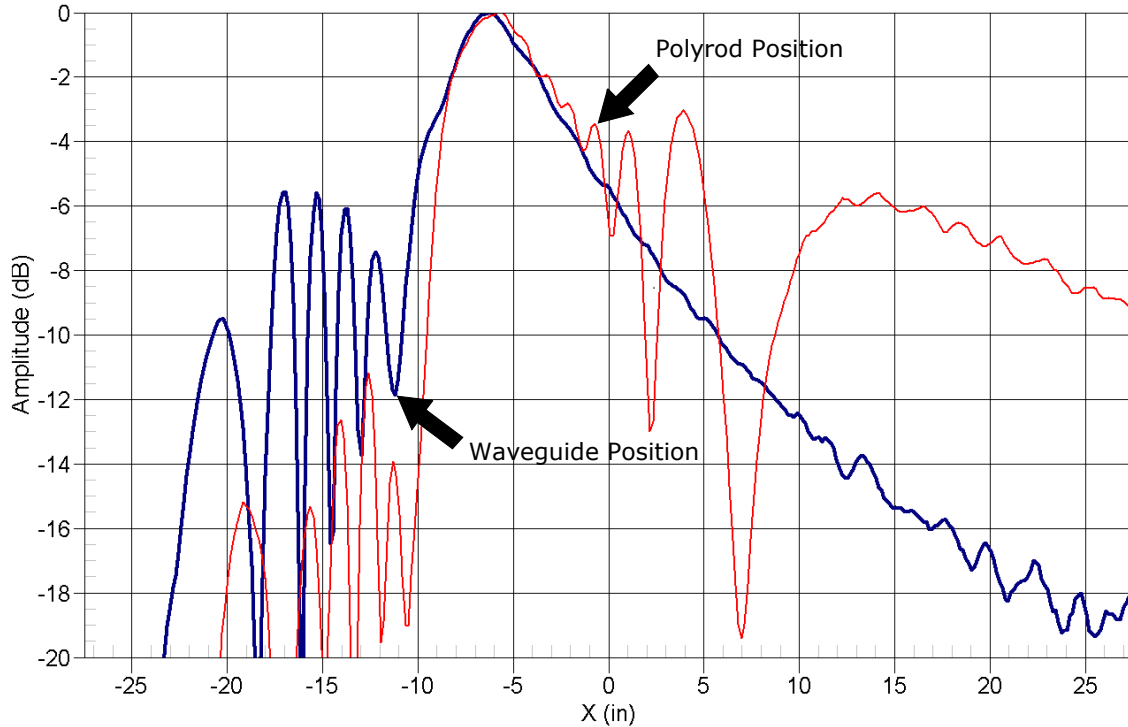
Figure 4.22: Magnitude cut along the x-axis of the WR-90 waveguide aperture (blue) and the polyrod antenna (red) at 7.5 GHz.

Figure 4.22 shows a magnitude cut of the waveguide (blue) and polyrod (red) antennas obtained from the near-field chamber. The test was performed in the near-field chamber by fixing the waveguide in a horizontal position with respect to the chamber floor and scanning along the length of the waveguide, offset from its side by several inches. In this way, the probe could be scanned behind the antenna aperture without colliding with the antenna. We can ascertain from this plot that the waveguide is located at approximately -11 in on the x-axis. The waveguide remained in this same position while testing the polyrod antenna, but the polyrod extends an additional 10 inches from the waveguide. Its tip, therefore, is located at approximately -1 in on the x-axis, as shown in the Figure 4.22.
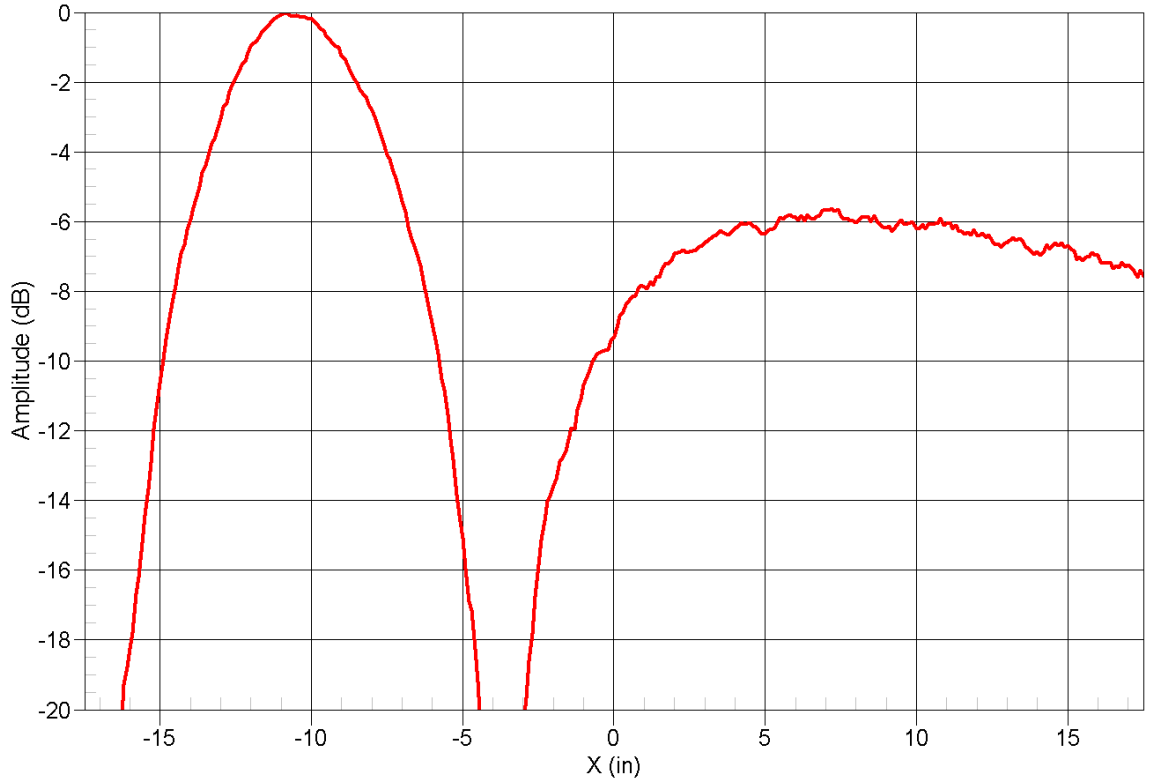
Figure 4.23: Magnitude cut along the x-axis of the SAQ-103039-90-S1 spot-focusing lens antenna at 10 GHz.

Figure 4.23 shows the same magnitude cut along the x-axis of the SAGE Millimeter, Inc. spot-focusing lens antenna. For this test, the antenna was positioned at approximately -16.5 in on the x-axis. We can see that it does produce a focused beam at approximately -9 in on the x-axis. With all the antenna locations determined, we can now compare the magnitude and phase of the three, as shown in Figure 4.24
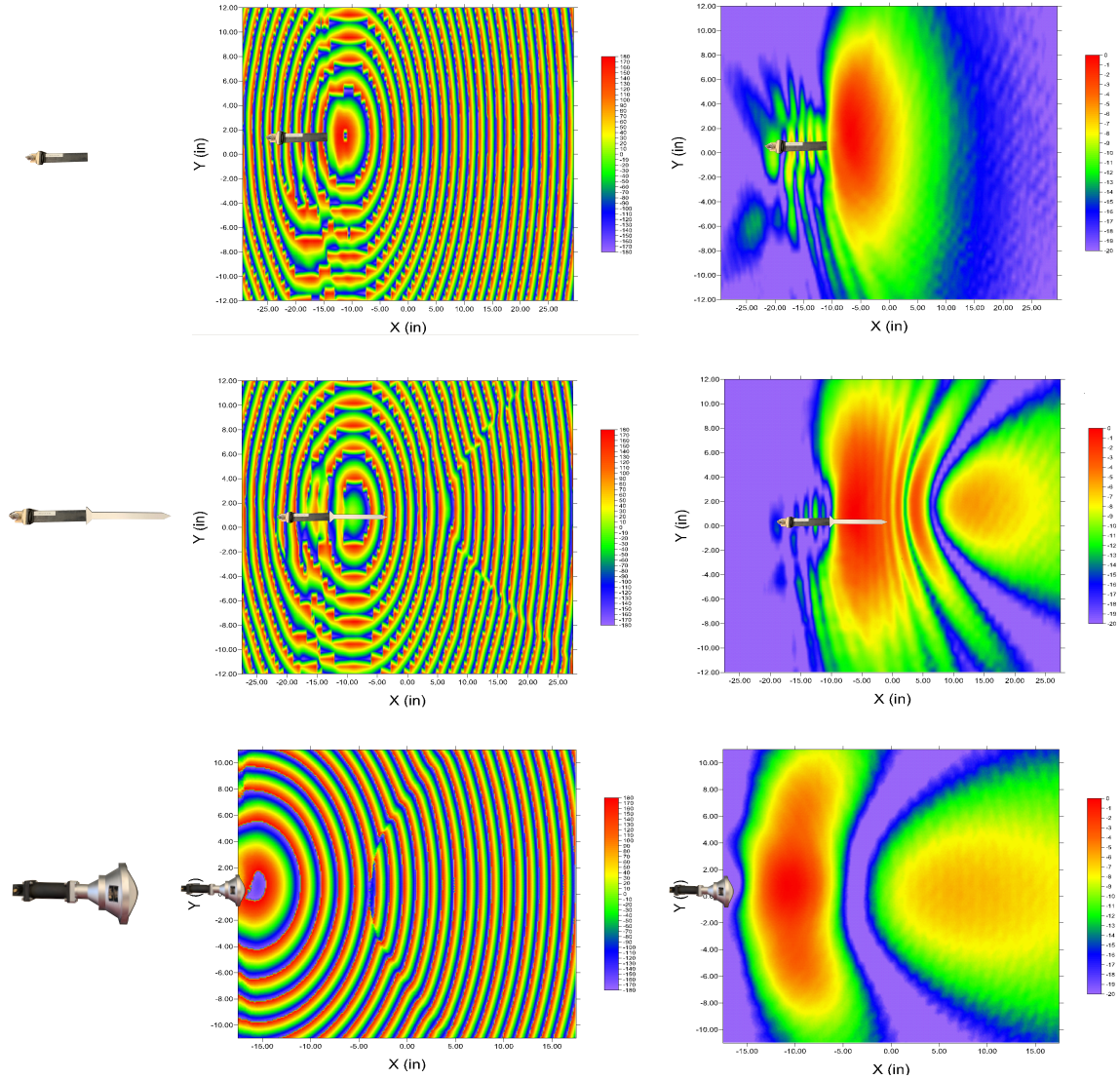
Figure 4.24: Magnitude and phase plots of the three antennas tested.

Comparing the magnitude plots for the three antennas, we can see that the polyrod produces a focused-beam at 4 in along the x-axis, or approximately 5 in from the tip of the polyrod antenna. However, the phase at this position is still very spherical. Since free-space material characterization requires a flat phase-front, this position is not suitable for measurement. The phase becomes much flatter around the 8-10 in position on the x-axis, corresponding to a distance of 9-11 in from the tip of the polyrod antenna. This was the distance used for testing, but produces a lower-power

beam. Additionally, the further the antenna is moved from the sample, the larger the sample must be to eliminate edge effects. The Sage Millimeter spot-focusing lens antenna produces a focused beam at -9 in on x-axis, corresponding to a distance of 7 in from the antenna. However, like the polyrod antenna, the phase at this distance is very spherical, even worse than the waveguide. Even at the maximum x-axis of 17 in, the phase is still not planar. This performance does not appear to meet the SAGE Millimeter spot-focusing lens antenna's own specifications, so an alternative focused-beam antenna that does produce a constant phase front at the focused beam position will need to be selected.

4.6   Summary

This chapter began by presenting the details of the LabVIEW drivers developed for each device controlled by the system. Next, the logic of the automatic calibration and data processing software was discussed for both the normal and oblique incidence cases and flowcharts of the software behavior were provided. A brief discussion of extraction algorithms followed, including the introduction of the clumsy, yet effective technique used here. Finally, materials characterization results were presented for Rogers 4350b, FR4 and a frequency-selective surface in both the normal and oblique incidence cases. The errors in the results were determined to be from non-ideal behavior from the polyrod antennas used and a commercial alternative antenna, along with the polyrod antennas and a WR-90 waveguide were tested in the near field chamber. The near-field chamber results showed that both the polyrod antennas and the SAGE Millimeter

spot-focusing lens antennas produced a focused beam, but did not have the required constant phase front at the focused beam location. In fact, the polyrod antennas produced a more constant phase front at a close distance than the spot-focusing lens antenna, although the polyrod antenna beam is fairly wide at this point. At larger angles of incidence tested during oblique characterization, the beam width becomes too large for the material samples presently used. The commercial antenna's beam width is even wider than the polyrod antennas at the distance where its phase-front is constant, so it also failed to meet the project requirements. Since no commercial antenna that meets these requirements and fits within the project budget could be found, a Gaussian focused-beam antenna will need to be designed in the next phase of the project.

Chapter 5

Conclusion

5.1 Epilogue

The existing anisotropic materials characterization instrument was successfully automated and its accuracy improved through hardware upgrades and custom software. The improved instrument was tested on Rogers 4350b, FR4 and an artificial dielectric, and found to still have some discrepancies with the expected results. The results were examined in detail for the error source, and the polyrod antennas were determined to be the main source of error. A suitable commercial replacement antenna was then selected and tested against the polyrod antennas in the near-field chamber. However, the commercial antenna had a worse performance than the polyrod antennas for the purposes of this project, and did not actually meet the specifications of their data sheets. Since other available commercial antennas that appeared to meet the project requirements were outside of the project budget, a Gaussian focused-beam antenna will need to be designed to replace the polyrod antennas in the next phase of the project.

5.1.1 Conclusion

The purpose of this project was to upgrade the existing anisotropic materials characterization instrument to improve its calibration process and allow convenient 2-D measurement of anisotropic materials. Several hardware upgrades were determined to be necessary before fully automated control of the system could be achieved. Appropriate off-the-shelf components were selected to perform these upgrades, or were fabricated in-house, like the P3 antenna bracket. Once all hardware upgrades were performed, custom Arduino firmware and LabVIEW software were written to automate the calibration and material characterization process. Once all software was written, the instrument was tested using Rogers 4350b, FR4, and an artificial dielectric material to validate its accuracy.

Although the measured magnitude of S_{21} values for the artificial dielectric and FR4 match with the expected values well, the measured magnitude of S_{11} values differ more significantly from the expected values, especially at greater angles of incidence. Additionally, the calculated permittivity and loss tangent values for FR4 contain more error than is desired. These errors likely come from a variety of sources, including mis-alignments of the sample holder and P3 antenna arm, deflection of the calibration standard and sample during testing, and positioning the calibration standard and the sample at positions slightly off from each other. However, the greatest source of error presently is the polyrod antennas. The antennas were tested in the near-field chamber and found to produce a much less constant phase front than was previously

thought. Since the free-space method requires a constant phase front to be accurate, this varying phase front introduces significant errors into the results.

After the polyrod antennas were identified as reducing the system accuracy, new SAQ-103039-90-S1 horn antennas equipped with a dielectric lens were selected to replace them. These antennas were specified to produce a 10 dB spot with a diameter of 2.09 inches at a focal length of 3.94 inches. They were tested in the near-field chamber to confirm that a Gaussian beam with a constant phase front was produced, and the results were compared to the polyrod antennas. It was determined that the antennas did produce a focused beam, but that the phase front of that focused beam was not at all planar, and therefore would not be a suitable replacement for this instrument. An antenna that produces a focused beam with constant phase and preferably a wide bandwidth is still needed to improve the instrument's accuracy.

5.1.2 Future Work

Several additional improvements will need to be made to the system in order to improve its accuracy. First, the polyrod antennas should be replaced with antennas using dielectric lenses, as previously discussed. The SAW-103039-90-S1 horn antennas using dielectric lenses were selected for this purpose but failed to meet their specifications. Additionally, either the four-parameter iterative method should be implemented in Matlab to process the collected data, or the sample holder should be redesign to ensure that the calibration standard and sample are always at the same position. Alternatively, any measuring system that allows the offset between the calibration standard and the sample to be measured will also allow this error to

be manually removed during post-processing. Finally, there is likely some error in the positioning of the P3 antenna arm relative to the sample's angle of incidence. The rotary tables were manually positioned using a laser level, but without a properly positioned limit switch to home the arms, some offset could be introduced after running multiple tests, which would increase the S_{11} error. These limit switches would also prevent the P3 antenna arm from being run into the other antenna arms, which could cause significant damage to the system.

Bibliography

[1] D. M. Pozar, *Microwave Engineering Fourth Edition*. 2005.

[2] A. Stringer, *A NOVEL METHOD FOR THE CHARACTERIZATION OF ANISOTROPIC MATERIALS*. PhD thesis, University of Oklahoma, 2018.

[3] Rogers Corporation, "RO4000 ® Series High Frequency Circuit Materials," 2006.

[4] J. W. Schultz, *Focused Beam Methods Measuring Microwave Materials in Free Space*. 2012.

[5] M. Kaniecki, E. Saenz, L. Rolo, R. Appleby, and O. Breinbjerg, "Scattering-parameter extraction and calibration techniques for RF free-space material characterization," in *8th European Conference on Antennas and Propagation, EuCAP 2014*, pp. 1093–1097, IEEE, apr 2014.

[6] G. F. Engen and C. A. Hoer, "Thru-Reflect-Line: An Improved Technique for Calibrating the Dual Six-Port Automatic Network Analyzer," *IEEE Transactions on Microwave Theory and Techniques*, vol. 27, pp. 987–993, dec 1979.

[7] H. J. Eul and B. Schiek, "A Generalized Theory and New Calibration Procedures for Network Analyzer Self-Calibration," *IEEE Transactions on Microwave Theory and Techniques*, vol. 39, pp. 724–731, apr 1991.

[8] H. J. Eul and B. Schiek, "Reducing the Number of Calibration Standards for Network Analyzer Calibration," *IEEE Transactions on Instrumentation and Measurement*, vol. 40, no. 4, pp. 732–735, 1991.

[9] U. Stumper, "Uncertainties of VNA S-Parameter Measurements Applying the TAN Self-Calibration Method," *IEEE Transactions on Instrumentation and Measurement*, vol. 56, pp. 597–600, apr 2007.

[10] U. Stumper and T. Schrader, "Influence of different configurations of nonideal calibration standards on vector network analyzer performance," *IEEE Transactions on Instrumentation and Measurement*, vol. 61, pp. 2034–2041, jul 2012.

[11] U. Stumper and T. Schrader, "Calibration method for vector network analyzers using one or two known reflection standards," *IEEE Transactions on Instrumentation and Measurement*, vol. 63, pp. 1648–1655, jun 2014.

[12] A. H. Muqaibel, *Characterization of Ultra Wideband Communication Channels*. PhD thesis, Virginia Polytechnic Institute and State University, 2003.

[13] L. J. A. Olule, G. Gnanagurunathan, and T. Nandha Kumar, "Electromagnetic metamaterial parameter retrieval methods: A review," in *RFM 2015 - 2015 IEEE International RF and Microwave Conference*, pp. 213–217, IEEE, dec 2016.

[14] A. M. Nicolson and G. F. Ross, "Measurement of the Intrinsic Properties Of Materials by Time-Domain Techniques," *IEEE Transactions on Instrumentation and Measurement*, vol. 19, pp. 377–382, nov 1970.

[15] W. B. Weir, "Automatic Measurement of Complex Dielectric Constant and Permeability at Microwave Frequencies," *Proceedings of the IEEE*, vol. 62, no. 1, pp. 33–36, 1974.

[16] D. R. Smith, D. C. Vier, T. Koschny, and C. M. Soukoulis, "Electromagnetic parameter retrieval from inhomogeneous metamaterials," *Physical Review E - Statistical, Nonlinear, and Soft Matter Physics*, vol. 71, p. 11, mar 2005.

[17] V. V. Varadan and R. Ro, "Unique retrieval of complex permittivity and permeability of dispersive materials from reflection and transmitted fields by enforcing causality," *IEEE Transactions on Microwave Theory and Techniques*, vol. 55, pp. 2224–2230, oct 2007.

[18] S. Kim, D. Novotny, J. Gordon, and J. Guerrieri, "A differential form of the Kramers-Kronig relation for determining a Lorentz-type of refractive index," in *IEEE Antennas and Propagation Society, AP-S International Symposium (Digest)*, vol. 2015-Octob, pp. 1174–1175, IEEE, jul 2015.

[19] I. B. Brezeanu, P. A. Paraschivoiu, R. Negroiu, and L. A. Chiva, "Applications of Kramers-Kronig Relations," in *2017 IEEE 23rd International Symposium for Design and Technology in Electronic Packaging (SIITME)*, pp. 82–85, IEEE, oct 2017.

[20] Z. Szabó, G. H. Park, R. Hedge, and E. P. Li, "A unique extraction of metamaterial parameters based on Kramers-Kronig relationship," *IEEE Transactions on Microwave Theory and Techniques*, vol. 58, pp. 2646–2653, oct 2010.

[21] J. J. Barroso and U. C. Hasar, "Comments on "A Unique Extraction of Metamaterial Parameters Based on Kramers-Kronig Relationship"," *IEEE Transactions on Microwave Theory and Techniques*, vol. 60, pp. 1743–1744, jun 2012.

[22] Z. Szabo, G. H. Park, R. Hedge, and E. P. Li, "Authors' Reply to "Comments on Unique Extraction of Metamaterial Parameters Based on Kramers–Kronig Relationship"," *IEEE Transactions on Microwave Theory and Techniques*, vol. 60, pp. 3634–3635, nov 2012.

[23] J. J. Barroso and U. C. Hasar, "Constitutive Parameters of a Metamaterial Slab Retrieved by the Phase Unwrapping Method," *Journal of Infrared, Millimeter, and Terahertz Waves*, vol. 33, pp. 237–244, feb 2012.

[24] A. Elhawil, G. Koers, L. Zhang, J. Stiens, and R. Vounckx, "Reliable method for material characterisation using quasi-optical free-space measurement in W-band," *IET Science, Measurement & Technology*, vol. 3, pp. 39–50, jan 2009.

[25] Baker-Jarvis and James, "Transmission/reflection and short-circuit line permittivity measurements," tech. rep., NIST, Washington, DC, 1990.

[26] U. C. Hasar, G. Buldu, Y. Kaya, and G. Ozturk, "Determination of effective constitutive parameters of inhomogeneous metamaterials with bianisotropy," *IEEE Transactions on Microwave Theory and Techniques*, vol. 66, pp. 3734–3744, aug 2018.

[27] H. Esteban, J. M. Catala, S. Cogollos, and V. E. Boria, "Characterization of complex dielectric properties of materials using a hybrid iterative method," in *IEEE Antennas and Propagation Society International Symposium: Wireless Technologies and Information Networks, APS 1999 - Held in conjunction with USNC/URSI National Radio Science Meeting*, vol. 10, pp. 186–188, may 2000.

[28] I. T. Rekanos, T. V. Yioultsis, and C. S. Hilas, "An inverse scattering approach based on the differential E-formulation," *IEEE Transactions on Geoscience and Remote Sensing*, vol. 42, pp. 1456–1461, jul 2004.

[29] R. A. Fenner and S. Keilson, "Free space material characterization using genetic algorithms," in *2014 16th International Symposium on Antenna Technology and Applied Electromagnetics (ANTEM)*, pp. 1–2, IEEE, jul 2014.

[30] A. Mancini, J. L. Salazar, R. M. Lebron, and B. L. Cheong, "A novel technique to characterize the effect of rain over a radome for radar applications," in *2017 IEEE Radar Conference (RadarConf)*, pp. 470–475, IEEE, may 2017.

[31] A. Mancini, J. L. Salazar, R. M. Lebrón, B. L. Cheong, A. Mancini, J. L. Salazar, R. M. Lebrón, and B. L. Cheong, "A Novel Instrument for Real-Time Measurement of Attenuation of Weather Radar Radome Including Its Outer Surface. Part I: The Concept," *Journal of Atmospheric and Oceanic Technology*, vol. 35, pp. 953–973, may 2018.

[32] A. Mancini, J. L. Salazar, R. M. Lebrón, B. L. Cheong, A. Mancini, J. L. Salazar, R. M. Lebrón, and B. L. Cheong, "A Novel Instrument for Real-Time Measurement of Attenuation of Weather Radar Radome Including Its Outer Surface. Part II: Applications," *Journal of Atmospheric and Oceanic Technology*, vol. 35, pp. 975–991, may 2018.

[33] U. Lundgren, *Characterization of Components and Materials for EMC Barriers*. PhD thesis, Lulea University of Technology, 2004.

[34] T. Ozturk, M. Hudlička, and Uluer, "Development of Measurement and Extraction Technique of Complex Permittivity Using Transmission Parameter S 21 for Millimeter Wave Frequencies," *Journal of Infrared, Millimeter, and Terahertz Waves*, vol. 38, pp. 1510–1520, dec 2017.

[35] F. Caspers, "RF Engineering Basic Concepts : S - Parameters," tech. rep., CERN, 2010.

[36] C. E. Kriegler, M. S. Rill, S. Linden, and M. Wegener, "Bianisotropic Photonic Metamaterials," *IEEE Journal of Selected Topics in Quantum Electronics*, vol. 16, no. 2, pp. 367–375, 2010.

[37] A. Dalkiliç, *ANALYSIS AND DESIGN OF CONFORMAL FREQUENCY SELECTIVE SURFACES A THESIS SUBMITTED TO THE GRADUATE SCHOOL OF NATURAL AND APPLIED SCIENCES OF MIDDLE EAST TECHNICAL UNIVERSITY*. PhD thesis, MIDDLE EAST TECHNICAL UNIVERSITY, 2014.

[38] D. Seetharamdoo, R. Sauleau, K. Mahdjoubi, and A. C. Tarot, "Anomalous frequency range of effective parameters of resonant negative refractive index metamaterials," in *ANTEM 2005 - 11th International Symposium on Antenna Technology and Applied Electromagnetics, Conference Proceedings*, pp. 1–4, IEEE, jun 2005.

[39] C. Menzel, C. Rockstuhl, T. Paul, F. Lederer, and T. Pertsch, "Retrieving effective parameters for metamaterials at oblique incidence," *Physical Review B*, vol. 77, p. 195328, may 2008.

[40] I. Rolfes and B. Schiek, "Calibration methods for microwave free space measurements," *Advances in Radio Science*, vol. 2, pp. 19–25, may 2005.

[41] A. N. Vicente, G. M. Dip, and C. Junqueira, "The step by step development of NRW method," in *2011 SBMO/IEEE MTT-S International Microwave and Optoelectronics Conference (IMOC 2011)*, pp. 738–742, IEEE, oct 2011.

[42] Raenita Fenner, *Error Analysis of Reflection-Only Material Characterization Methods*. PhD thesis, Michigan State University, 2011.

[43] M. G. Silveirinha, "Generalized Lorentz-Lorenz formulas for microstructured materials," *Physical Review B*, vol. 76, p. 245117, dec 2007.

[44] K. Buell, *Development of Engineered Magnetic Materials for Antenna Applications*. PhD thesis, University of Michigan, 2005.

[45] K. Saeed, R. D. Pollard, and I. C. Hunter, "Substrate integrated waveguide cavity resonators for complex permittivity characterization of materials," *IEEE Transactions on Microwave Theory and Techniques*, vol. 56, pp. 2340–2347, oct 2008.

[46] P. G. Bartley and S. B. Begley, "A new free-space calibration technique for materials measurement," in *2012 IEEE International Instrumentation and Measurement Technology Conference Proceedings*, (Graz, Austria), pp. 47–51, IEEE, may 2012.

[47] H. J. Lee, H. S. Lee, P. S. Ma, and Y. Y. Kim, "Effective material parameter retrieval of anisotropic elastic metamaterials with inherent nonlocality," *Journal of Applied Physics*, vol. 120, p. 104902, sep 2016.

[48] L. E. Rickard Petersson and G. S. Smith, "On the use of a Gaussian beam to isolate the edge scattering from a plate of finite size," *IEEE Transactions on Antennas and Propagation*, vol. 52, pp. 505–512, feb 2004.

[49] P. F. Goldsmith, *Quasioptical systems: Gaussian beam quasioptical propagation and applications*. IEEE Press, 1998.

[50] A. Solovey, M. Wasson, and R. Mittra, "Free space transmission loss measurement of magneto-dielectric materials: Solution uniqueness and measurement tolerance tradeoffs," in *The 40th European Microwave Conference*, (Paris, France), IEEE, 2010.

[51] M. A. Silaghi, ed., *Dielectric Material*. InTech, oct 2012.

[52] R. A. Fenner, E. J. Rothwell, and L. L. Frasch, "A comprehensive analysis of free-space and guided-wave techniques for extracting the permeability and permittivity of materials using reflection-only measurements," *Radio Science*, vol. 47, feb 2012.

[53] A. M. Hassan, J. Obrzut, and E. J. Garboczi, "A Q-Band Free-Space Characterization of Carbon Nanotube Composites," *IEEE Transactions on Microwave Theory and Techniques*, vol. 64, pp. 3807–3819, nov 2016.

[54] D. Cohen and R. Shavit, "Bi-anisotropic Metamaterials Effective Constitutive Parameters Extraction Using Oblique Incidence S-Parameters Method," *IEEE Transactions on Antennas and Propagation*, vol. 63, pp. 2071–2078, may 2015.

[55] S. K. Ghosh, S. K. Parui, and A. Chatterjee, "Development of novel engineered metamaterial: Structure, extraction of various parameters and applications," in *2017 1st International Conference on Electronics, Materials Engineering and Nano-Technology, IEMENTech 2017*, pp. 1–6, IEEE, apr 2017.

[56] H. S. Sehmi, W. Langbein, and E. A. Muljarov, "Optimizing the drude-lorentz model for material permittivity: Examples for semiconductors," in *Progress in Electromagnetics Research Symposium*, pp. 994–1000, 2017.

[57] H.-C. Yin, Z.-M. Chao, and Y.-P. Xu, "A new free-space method for measurement of electromagnetic parameters of biaxial materials at microwave frequencies," *Microwave and Optical Technology Letters*, vol. 46, pp. 72–78, jul 2005.

[58] C. Menzel, C. Rockstuhl, T. Paul, T. Pertsch, and F. Lederer, "Effective Parameters For Anisotropic Metamaterials," in *Conference on Lasers and Electro-Optics/International Quantum Electronics Conference*, (Washington, D.C.), pp. 1–2, OSA, 2009.

[59] A. G. Knisely and M. J. Havrilla, "Material characterization de-embedding for rectangular to square waveguide," in *Antennas and Propagation (EuCAP), 2015 9th European Conference on.*, (Lisbon, Portugal), pp. 1–5, IEEE, 2015.

[60] R. T. Johnk and A. Ondrejka, "Electrical material properties from a free-space time-domain RF absorber reflectivity measurement system," in *IEEE 1997, EMC, Austin Style. IEEE 1997 International Symposium on Electromagnetic Compatibility. Symposium Record (Cat. No.97CH36113)*, pp. 537–542, IEEE, 1997.

[61] C. A. Gonano and R. E. Zich, "Drude-Lorentz model in circuit form," in *8th European Conference on Antennas and Propagation, EuCAP 2014*, pp. 1518–1521, IEEE, apr 2014.

[62] J. Obrzut, A. M. Hassan, and E. J. Garboczi, "Free Space Microwave Non Destructive Characterization of Composite Materials — NIST," in *NDT of Composites 2015*, vol. 2015, NIST, may 2015.

[63] D. K. Ghodgaonkar, V. V. Varadan, and V. K. Varadan, "A free-space method for measurement of dielectric constants and loss tangents at microwave frequencies," *IEEE Transactions on Instrumentation and Measurement*, vol. 38, pp. 789–793, jun 1989.

[64] J. Shin, A. Akyurtlu, M. Deshpande, and R. W. Ziolkowski, "Comments on "design, fabrication, and testing of double negative metamaterials"," feb 2005.

[65] T. D. Karamanos and N. V. Kantartzis, "Effective parameter retrieval of 3D bianisotropic scatterer arrays for oblique propagation," in *2016 10th International Congress on Advanced Electromagnetic Materials in Microwaves and Optics, METAMATERIALS 2016*, pp. 154–156, IEEE, sep 2016.

[66] J. L. Vedral, *Analysis, Characterization and Application of Microwave Metamaterials.* PhD thesis, University of Colorado at Colorado Springs, 2016.

[67] A. G. Knisely, M. W. Hyde, M. J. Havrilla, and P. J. Collins, "Uniaxial anisotropic material measurement using a single port waveguide probe," in *AMTA 2016 Proceedings*, (Austin, TX, USA), pp. 1–6, IEEE, oct 2016.

[68] Kai Du, *Permittivity Measurement of Circular Shell Using a Spot-Focused Free-Space System and Reflection Analysis of Open-ended Coaxial Line Radiating into a Chiral Medium.* PhD thesis, Pennsylvania State University, 2001.

[69] S. Kim, E. F. Kuester, C. L. Holloway, A. D. Scher, and J. R. Baker-Jarvis, "EFFECTIVE MATERIAL PROPERTY EXTRACTION OF A METAMATERIAL BY TAKING BOUNDARY EFFECTS INTO ACCOUNT AT TE/TM POLARIZED INCIDENCE," *Progress In Electromagnetics Research B*, vol. 36, pp. 1–33, 2012.

[70] C. E. Kintner, *Free-Space Measurements of Dielectrics and Three-Dimensional Periodic Metamaterials.* PhD thesis, University of Arkansas, 2017.

[71] B. P. Mishra, S. Sahu, S. K. Pathak, and S. K. S. Parashar, "An investigation on cross-shaped fishnet metamaterial for W-band radar application," in *2017 IEEE Calcutta Conference, CALCON 2017 - Proceedings*, vol. 2018-Janua, pp. 314–317, IEEE, dec 2018.

[72] W. Fwen, S. Ping, M. F. Abd Malek, and N. Hasss, "Alternatives for PCB Laminates: Dielectric Properties' Measurements at Microwave Frequencies," in *Dielectric Material* (M. I. Silaghi, ed.), ch. 5, InTech, oct 2012.

[73] J. Qi, H. Kettunen, H. Wallen, and A. Sihvola, "Different homogenization methods based on scattering parameters of dielectric-composite slabs," *Radio Science*, vol. 46, no. 5, pp. 1–7, 2011.

[74] E. Kemptner and S. Thurner, "Free space material characterization for microwave frequencies," in *2012 6th European Conference on Antennas and Propagation (EUCAP)*, pp. 3513–3515, IEEE, mar 2012.

[75] R. W. Ziolkowski, "Design, fabrication, and testing of double negative metamaterials," *IEEE Transactions on Antennas and Propagation*, vol. 51, pp. 1516–1529, jul 2003.

[76] S. Roberts and A. Von Hippel, "A New Method for Measuring Dielectric Constant and Loss in the Range of Centimeter Waves," *Journal of Applied Physics*, vol. 17, pp. 610–616, jul 1946.

[77] C. C. Njoku, W. G. Whittow, and J. C. Vardaxoglou, "Simulation Methodology for Synthesis of Antenna Substrates With Microscale Inclusions," *IEEE Transactions on Antennas and Propagation*, vol. 60, pp. 2194–2202, may 2012.

[78] R. A. Fenner and E. J. Rothwell, "Deficiency in the error propagation method for sensitivity analysis of free space material characterization," in *Antenna Technology and Applied Electromagnetics (ANTEM), 2012 15th International Symposium on*, no. 1, pp. 1–3, IEEE, jun 2012.

[79] R. Feio, *Material Parameter Extraction from Reflection Measurements.* PhD thesis, Universidade do Porto, 2017.

[80] Ó. García-Pérez, F. Tercero, and S. López-Ruiz, "Free-space W-band setup for the electrical characterization of materials and mm-wave components," tech. rep., 2017.

[81] I. Zivkovic and A. Murk, "Free-Space Transmission Method for the Characterization of Dielectric and Magnetic Materials at Microwave Frequencies," in *Microwave Materials Characterization*, ch. 5, InTech, nov 2012.

[82] A. Solovey, M. Wasson, and R. Mittra, "Measurement of Conductive Magneto-Dielectric Material Parameters in High Noise Environment," in *2011 41st European Microwave Conference*, (Manchester, UK), IEEE, 2011.

[83] D. Zaluški, A. Grbic, and S. Hrabar, "Analytical and experimental characterization of metasurfaces with normal polarizability," *Physical Review B*, vol. 93, p. 155156, apr 2016.

[84] H. Wei, S. Lihua, X. Qiwei, and L. Feng, "Shielding effectiveness estimation for concrete slabs based on measured frequency dependent dielectric constant," in *2015 7th Asia-Pacific Conference on Environmental Electromagnetics (CEEM)*, pp. 309–312, IEEE, nov 2015.

[85] A.-S. Popescu, I. Bendoym, T. Rexhepi, and D. Crouse, "ANISOTROPIC ZERO INDEX MATERIAL: A METHOD OF REDUCING THE FOOTPRINT OF VIVALDI ANTENNAS IN THE UHF RANGE," *Progress In Electromagnetics Research C*, vol. 65, pp. 33–43, 2016.

[86] D. R. Smith, S. Schultz, P. Markoš, and C. M. Soukoulis, "Determination of effective permittivity and permeability of metamaterials from reflection and transmission coefficients," *Physical Review B*, vol. 65, no. 19, p. 5, 2002.

[87] S. Arslanagić, T. V. Hansen, N. A. Mortensen, A. H. Gregersen, O. Sigmund, R. W. Ziolkowski, and O. Breinbjerg, "A review of the scattering-parameter extraction method with clarification of ambiguity issues in relation to metamaterial homogenization," *IEEE Antennas and Propagation Magazine*, vol. 55, pp. 91–106, apr 2013.

[88] A. Solovey and R. Mittra, "Measurement of thin conductive dielectric coating material parameters in a high noise environment," *International Journal of RF and Microwave Computer-Aided Engineering*, vol. 23, pp. 452–458, jul 2013.

[89] F. Costa, M. Borgese, M. Degiorgi, and A. Monorchio, "Electromagnetic Characterisation of Materials by Using Transmission/Reflection (T/R) Devices," *Electronics*, vol. 6, p. 95, nov 2017.

[90] L. C. Paul, M. A. Haque, M. A. Haque, M. M. U. Rashid, M. F. Islam, and M. M. Rahman, "Design a slotted metamaterial microstrip patch antenna by creating three dual isosceles triangular slots on the patch and bandwidth enhancement," in *2017 3rd International Conference on Electrical Information and Communication Technology (EICT)*, pp. 1–6, IEEE, dec 2017.

[91] X. Zhang, T. Chang, H. L. Cui, Z. Sun, C. Yang, X. Yang, L. Liu, and W. Fan, "A Free-Space Measurement Technique of Terahertz Dielectric Properties," *Journal of Infrared, Millimeter, and Terahertz Waves*, vol. 38, pp. 356–365, mar 2017.

[92] R. W. Ziolkowski, "Author reply to comments on "Design, fabrication, and testing of double negative metamaterials"," *Antennas and Propagation, IEEE Transactions on*, vol. 53, pp. 891–892, feb 2005.

[93] A. Castanié, J.-F. Mercier, S. Félix, and A. Maurel, "Generalized method for retrieving effective parameters of anisotropic metamaterials," *Optics Express*, vol. 22, no. 24, 2014.

[94] S. J. Orfanidis, *Electromagnetic Waves and Antennas*. 2004.

[95] X. Huang, S. Yu, J. Chen, and H. Yang, "Ultra broadband metamaterial absorber with oblique incidence based on effective medium theory," in *ISAPE 2016 - Proceedings of the 11th International Symposium on Antennas, Propagation and EM Theory*, pp. 1–4, IEEE, oct 2017.

[96] C. A. Balanis, *Advanced engineering electromagnetics*. John Wiley & Sons, second edi ed., 2012.

[97] Z. Cui, Y. Han, and H. Zhang, "Scattering of an arbitrarily incident focused Gaussian beam by arbitrarily shaped dielectric particles," *Journal of the Optical Society of America B*, vol. 28, pp. 2625–2632, nov 2011.

[98] B. Crowgey, J. Tang, O. Tuncer, L. Kempel, E. Rothwell, and B. Shanker, "Measurement of anisotropic material properties for antenna applications," in *2012 Loughborough Antennas & Propagation Conference (LAPC)*, pp. 1–4, IEEE, nov 2012.

[99] T. Martin and B. Vallhagen, "A novel method to increase the accuracy of material characterization using free space transmission measurements," in *2017 International Conference on Electromagnetics in Advanced Applications (ICEAA)*, pp. 1608–1611, IEEE, sep 2017.

[100] R. J. Wylde, G. S. Bell, and A. Murk, "Sample size limitations for frequency-swept free-space material characterization," in *2012 37th International Conference on Infrared, Millimeter, and Terahertz Waves*, p. 1, IEEE, sep 2012.

[101] J. Schultz, J. Maloney, K. Maloney, and R. Schultz, "A Comparison of Material Measurement Accuracy of RF Spot Probes to a Lens-Based Focused Beam System," in *AMTA 36th Annual Meeting and Symposium*, 2014.

[102] L. S. Bobrow, *Elementary linear circuit analysis*. New York: Holt, Rinehart, and Winston, 2nd ed. ed., 1987.

[103] A. N. Plastikov, "About two approaches to automation of a process of calculating metamaterial parameters according to the scattering-parameter extraction method using modern full-wave simulators," in *2017 Progress In Electromagnetics Research Symposium - Spring (PIERS)*, pp. 3763–3767, IEEE, may 2017.

[104] X. Chen, T. M. Grzegorczyk, B. I. Wu, J. Pacheco, and J. A. Kong, "Robust method to retrieve the constitutive effective parameters of metamaterials," *Physical Review E - Statistical Physics, Plasmas, Fluids, and Related Interdisciplinary Topics*, vol. 70, no. 1, p. 7, 2004.

[105] A. G. Knisely, *Biaxial Anisotropic Material Development and Characterization using Rectangular to Square Waveguide.* PhD thesis, AIR FORCE INSTITUTE OF TECHNOLOGY, 2015.

[106] V. V. Varadan and Z. Sheng, "Direct Comparison of the Magnitude and Phase of Measured S-parameters of Metamaterials with Finite Element Simulation," in *2006 IEEE Antennas and Propagation Society International Symposium*, pp. 4587–4590, IEEE, 2006.

[107] J.-Y. Chung, *Broadband Characterization Techniques for RF Materials and Engineered Composites.* PhD thesis, Ohio State University, 2010.

[108] X. Chen, B.-I. Wu, J. A. Kong, and T. M. Grzegorczyk, "Retrieval of the effective constitutive parameters of bianisotropic metamaterials," *Physical Review E*, vol. 71, p. 46610, apr 2005.

[109] "Basics of Measuring the Dielectric Properties of Materials," tech. rep., Application Note 5989-2589EN, Keysight Technologies, 2017.

[110] A. Alù, "First-principles homogenization theory for periodic metamaterials," *Physical Review B*, vol. 84, p. 75153, aug 2011.

[111] Y. Si and Z. Zhan, "Extraction of metamaterial parameters," in *2015 IEEE 6th International Symposium on Microwave, Antenna, Propagation, and EMC Technologies, MAPE 2015*, pp. 608–610, IEEE, oct 2016.

[112] P. Paul, F. G. Guimarães, and J. P. Webb, "Reducing the computational cost of inverse scattering problems with evolutionary algorithms," *IEEE Transactions on Magnetics*, vol. 45, pp. 1514–1517, mar 2009.

[113] V. V. Varadan, S. Puligalla, and R. Ro, "S-parameter measurements for oblique angles of incidence and Brewster angle studies for metamaterial samples," *Microwave and Optical Technology Letters*, vol. 48, pp. 2619–2624, dec 2006.